Journal of Sound and Vibration (1991) **144**(3), 469–506

NON-LINEAR DYNAMICS OF A GEARED ROTOR–BEARING SYSTEM WITH MULTIPLE CLEARANCES

A. KAHRAMAN† AND R. SINGH

Department of Mechanical Engineering, The Ohio State University, 206 West 18th Avenue, Columbus, Ohio 43210-1107, U.S.A.

(*Received* 30 *October* 1989, *and in final form* 9 *April* 1990)

Non-linear frequency response characteristics of a geared rotor-bearing system are examined in this paper. A three-degree-of-freedom dynamic model is developed which includes non-linearities associated with radial clearances in the radial rolling element bearings and backlash between a spur gear pair; linear time-invariant gear meshing stiffness is assumed. The corresponding linear system problem is also solved, and predicted natural frequencies and modes match with finite element method results. The bearing non-linear stiffness function is approximated for the sake of convenience by a simple model which is identical to that used for the gear mesh. This approximate bearing model has been verified by comparing steady state frequency spectra. Applicability of both analytical and numerical solution techniques to the multi-degree-of-freedom non-linear problem is investigated. Satisfactory agreement has been found between our theory and available experimental data. Several key issues such as non-linear modal interactions and differences between internal static transmission error excitation and external torque excitation are discussed. Additionally, parametric studies are performed to understand the effect of system parameters such as bearing stiffness to gear mesh stiffness ratio, alternating to mean force ratio and radial bearing preload to mean force ratio on the non-linear dynamic behavior. A criterion used to classify the steady state solutions is presented, and the conditions for chaotic, quasi-periodic and subharmonic steady state solutions are determined. Two typical routes to chaos observed in this geared system are also identified.

1. INTRODUCTION

Mathematical modeling of geared rotor–bearing systems, being an essential step in designing quiet and reliable power transmissions, has been the subject of numerous studies over the past few decades. Most of the proposed dynamic models, as reviewed by Ozguven and Houser [1], are essentially linear. However, in several cases, it has been experimentally shown that the geared systems exhibit non-linear behavior [2-5]. For instance, vibro-impacts are observed in a lightly loaded transmission with gear backlash or loose bearings [6-8]. Accordingly, one must develop a non-linear mathematical model of the geared system: this is the main focus of this paper, with emphasis on the clearance-type non-linearity in gears and rolling element bearings. In a recent paper [9] we considered the single-degree-of-freedom non-linear model of a spur gear pair with backlash, and investigated the effects of system parameters on the vibrations and chaos excited by the static transmission error. Applicability of the harmonic balance method and digital simulation technique to the solution of the steady state response has been demonstrated, and difficulties associated with the digital simulation technique when applied to such systems governed by stiff non-linear differential equations have been resolved [9].

†Currently with the General Motors Research Laboratories, Power Systems Research Department, 30500 Mound Road, Warren, Michigan 48090-9055, U.S.A.

0022-460X/91/030469+38 $03.00/0

Although there is a vast body of literature concerned with a single-degree-of-freedom system with clearances, as reviewed earlier in reference [9], studies on multi-degree-of-freedom vibro-impact systems are very limited. For example, Galhoud *et al.* [10] considered a two-degree-of-freedom translational system with a gap and found the forced harmonic response using the piecewise linear technique. Winter and Kojima [11] also used the same technique to study geared systems with backlash. However, it should be noted that the picewise linear technique cannot predict several non-linear phenomena such as subharmonic and chaotic responses since it is based on the assumption that both impact and no-impact regimes "are repeated in an identical manner once every period of excitation" [10]. Kucukay [5] developed an eight-degree-of-freedom model of a helical gear pair with backlash to include the rocking and axial motions of rigid shafts and radial deflections of linear bearings. Lin *et al.* [12] included motor and load inertias in a three-degree-of-freedom torsional model. In both of these studies the digital simulation technique was used, but a number of issues of primary concern in non-linear system such as the existence of multiple steady state solutions, their dependence on initial conditions, subharmonic, quasi-periodic and chaotic responses, etc., were not considered. A few of these issues have been addressed by Singh *et al.* [8] on the gear rattle problem. Comparin and Singh [13] have also used digital simulation, analog simulation and the harmonic balance method to analyze coupled impact pairs assuming that the modes are "weakly coupled", which allows the system to be represented by a combination of single impact pairs. They included only the low-frequency external torque excitation and found the steady state frequency response at the primary resonance. This solution was then used to analyze the neutral gear problem more in detail [14].

The other two groups of studies concerned with multi-degree-of-freedom systems with continuous non-linearities [15–20] and periodic excitations due to mesh stiffness variations [4, 21] will not be addressed here since their responses are significantly different from the clearance non-linearities, as discussed by Comparin and Singh [22]. The literature on chaotic vibrations and rolling element bearings will be discussed later.

2. PROBLEM FORMULATION

2.1. SCOPE

The generic geared system considered in this study is shown in Figure 1. It consists of a spur gear pair mounted on flexible shafts which are supported by rolling element bearings assembled in a rigid gearbox. Since the shafts and bearings are compliant, our single-degree-of-freedom model of spur gear pair [9] with gear centers assumed fixed is obviously not suitable. Instead, a three-degree-of-freedom non-linear model as shown in Figure 2(a) is considered. It includes equivalent stiffness and damping elements representing the shaft and the bearings. The corresponding linear model has been found to be sufficiently accurate when compared with a finite element model for eigensolutions [23] provided that the gear dynamic response (mesh force, dynamic transmission error, etc.) is of major concern. Gear backlash and radial clearances in bearings are defined analytically. An approximate non-linear bearing model is also proposed. Applicability of both analytical and numerical solution techniques to this problem is investigated. Several key issues such as non-linear modal interactions and differences between internal static transmission error excitation and external torque excitation are discussed. Parametric studies are conducted to understand the effect of system parameters such as bearing stiffness k_{bi} to mesh stiffness k_h ratio $\hat{k} = k_{bi}/k_h$, alternating to mean force ratio F_a/F_m and radial bearing preload to mean force ratio F_b/F_m on the non-linear frequency response. A criterion is used to classify the steady state solutions, and the conditions for chaotic, quasi-periodic and subharmonic steady state solutions are determined. Two

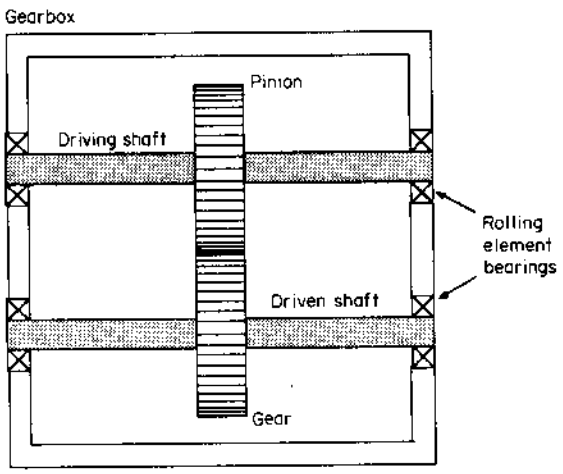

Figure 1. Generic geared rotor-bearing system.

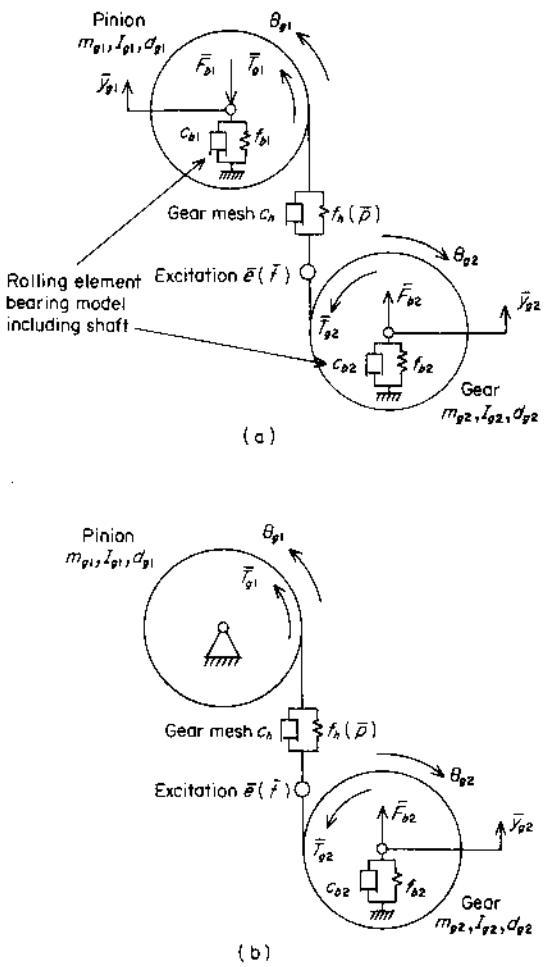

Figure 2. Non-linear models of the geared rotor-bearing system; (a) three-degree-of-freedom model, (b) two-degree-of-freedom model.

typical routes to chaos observed on a geared system are also identified. Finally, our formulation is verified by comparing predictions with measurements [2].

2.2. PHYSICAL MODEL AND ASSUMPTIONS

The three-degree-of-freedom non-linear model of the geared rotor system with gear inertias I_{g1} and I_{g2}, gear masses m_{g1} and m_{g2}, and base circle diameters d_{g1} and d_{g2}, as shown in Figure 2(a), is considered here. The gear mesh is described by a non-linear displacement function f_h and viscous damping c_h. Friction forces at the mesh point are assumed to be negligible [24]. Thus the transverse vibrations in the pressure line direction are uncoupled from the vibrations in the direction perpendicular to the pressure line. Bearings and the shafts that support the gears are modeled by equivalent elements with viscous damping coefficients c_{b1} and c_{b2} and non-linear springs defined by force-displacement functions f_{b1} and f_{b2}. The effects of the prime mover and the load inertias are not considered, assuming that these inertial elements are connected to the gearbox through soft torsional couplings. Further, it is assumed that the system is symmetric about the plane of the gears and that the axial motion (parallel to the shafts) is negligible. Like our previous spur gear pair model [9], both low-frequency external excitation due to torque fluctuations and high-frequency internal excitations due to the static transmission error $\bar{e}(\bar{t})$ are considered in the formulation. Input torque fluctuation is included, but the output torque is assumed to be constant: i.e. $\bar{T}_{g1}(\bar{t}) = \bar{T}_{g1m} + \bar{T}_{g1a}(\bar{t})$ and $\bar{T}_{g2}(\bar{t}) = \bar{T}_{g2m}$. External radial preloads $\bar{F}_{b1}$ and $\bar{F}_{b2}$ are also applied to both rolling element bearings. (A list of symbols is given in the Appendix.)

2.3. EQUATIONS OF MOTION

Equations of coupled transverse-torsional motion of the non-linear geared rotor-bearing system shown in Figure 2(a) are

$$m_{g1}\bar{y}''_{g1} + c_{b1}\bar{y}'_{g1} + c_h(\bar{x}' + \bar{y}'_{g1} - \bar{y}'_{g2} - \bar{e}') + k_{b1}f_{b1}(\bar{y}_{g1}) + k_h f_h(\bar{x} + \bar{y}_{g1} - \bar{y}_{g2} - \bar{e}) = -\bar{F}_{b1}, \quad (1a)$$

$$m_{g2}\bar{y}''_{g2} + c_{b2}\bar{y}'_{g2} - c_h(\bar{x}' + \bar{y}'_{g1} - \bar{y}'_{g2} - \bar{e}') + k_{b2}f_{b2}(\bar{y}_{g2}) - k_h f_h(\bar{x} + \bar{y}_{g1} - \bar{y}_{g2} - \bar{e}) = \bar{F}_{b2}, \quad (1b)$$

$$m_{c1}\bar{x}'' + c_h(\bar{x}' + \bar{y}'_{g1} - \bar{y}'_{g2} - \bar{e}') + k_h f_h(\bar{x} + \bar{y}_{g1} - \bar{y}_{g2} - \bar{e}) = \bar{F}_m + \bar{F}_{aT}(\bar{t}), \quad (1c)$$

$$\bar{x}(\bar{t}) = \frac{d_{g1}}{2}\theta_{g1}(\bar{t}) - \frac{d_{g2}}{2}\theta_{g2}(\bar{t}), \qquad m_{c1} = 1\Big/\left(\frac{d_{g1}^2}{4I_{g1}} + \frac{d_{g2}^2}{4I_{g2}}\right), \quad (1d, e)$$

$$\bar{F}_m = 2\bar{T}_{g1m}/d_{g1} = 2\bar{T}_{g2m}/d_{g2}, \qquad \bar{F}_{aT}(\bar{t}) = m_{c1}\bar{T}_{g1a}(\bar{t})/2I_{g1}. \quad (1f, g)$$

Here, $(\,)'$ means derivative with respect to time $\bar{t}$, y_{gi} and θ_{gi} are the transverse and torsional displacements of the ith gear ($i = 1, 2$), m_{c1} is the equivalent gear pair mass, $\bar{F}_m$ is the average force transmitted through the gear mesh and $\bar{F}_{aT}(t)$ is the fluctuating force related to the external input torque excitation. Equations (1a)-(1c) are simplified further by defining below a new variable $\bar{p}(\bar{t})$ which is the difference between the dynamic transmission error and the static transmission error $\bar{e}(\bar{t})$:

$$\bar{p}(\bar{t}) = \bar{x}(\bar{t}) + \bar{y}_{g1}(\bar{t}) - \bar{y}_{g2}(\bar{t}) - \bar{e}(\bar{t}), \quad (2a)$$

$$\begin{bmatrix} m_{g1} & 0 & 0 \\ 0 & m_{g2} & 0 \\ -m_{c1} & m_{c1} & m_{c1} \end{bmatrix} \begin{Bmatrix} \bar{y}''_{g1}(\bar{t}) \\ \bar{y}''_{g2}(\bar{t}) \\ \bar{p}''(\bar{t}) \end{Bmatrix} + \begin{bmatrix} c_{b1} & 0 & c_h \\ 0 & c_{b2} & -c_h \\ 0 & 0 & c_h \end{bmatrix} \begin{Bmatrix} \bar{y}'_{g1}(\bar{t}) \\ \bar{y}'_{g2}(\bar{t}) \\ \bar{p}'(\bar{t}) \end{Bmatrix} + \begin{bmatrix} k_{b1} & 0 & k_h \\ 0 & k_{b2} & -k_h \\ 0 & 0 & k_h \end{bmatrix} \begin{Bmatrix} f_{b1}(\bar{y}_{g1}) \\ f_{b2}(\bar{y}_{g2}) \\ f_h(\bar{p}) \end{Bmatrix}$$

$$= \begin{Bmatrix} -\bar{F}_{b1} \\ \bar{F}_{b2} \\ \bar{F}_m - m_{c1}\bar{e}''(\bar{t}) + \bar{F}_{aT}(\bar{t}) \end{Bmatrix}. \quad (2b)$$

A dimensionless form of equation (2b) is obtained by letting $y_{gi}(\bar{t}) = \bar{y}_{gi}(\bar{t})/b_c$, $p(\bar{t}) = \bar{p}(\bar{t})/b_c$, $\omega_n = \sqrt{k_h/m_{c1}}$, $\omega_{bi} = \sqrt{k_{bi}/m_{gi}}$ $(i = 1, 2)$ and $t = \omega_n \bar{t}$, where b_c is the characteristic length. Here, harmonic excitation is considered for both $\bar{e}(\bar{t})$ and $\bar{F}_{aT}(\bar{t})$, with $\bar{e}(\bar{t}) = \tilde{e} \sin(\bar{\Omega}_h \bar{t} + \phi_h)$, $\bar{F}_{aT}(\bar{t}) = \tilde{F}_{aT} \sin(\bar{\Omega}_T \bar{t} + \phi_T)$, where $\bar{\Omega}_h$ and $\bar{\Omega}_T$ are the fundamental excitation frequencies of internal displacement and external torque fluctuations, respectively. Further, dimensionless excitation frequencies $\Omega_h = \bar{\Omega}_h/\omega_n$ and $\Omega_T = \bar{\Omega}_T/\omega_n$ are defined to yield the following dimensionless governing equation of motion:

$$\begin{bmatrix} 1 & 0 & 0 \\ 0 & 1 & 0 \\ -1 & 1 & 1 \end{bmatrix} \begin{Bmatrix} \ddot{y}_{g1}(t) \\ \ddot{y}_{g2}(t) \\ \ddot{p}(t) \end{Bmatrix} + 2 \begin{bmatrix} \zeta_{11} & 0 & \zeta_{13} \\ 0 & \zeta_{22} & -\zeta_{23} \\ 0 & 0 & \zeta_{33} \end{bmatrix} \begin{Bmatrix} \dot{y}_{g1}(t) \\ \dot{y}_{g2}(t) \\ \dot{p}(t) \end{Bmatrix} + \begin{bmatrix} \kappa_{11} & 0 & \kappa_{13} \\ 0 & \kappa_{22} & -\kappa_{23} \\ 0 & 0 & 1 \end{bmatrix} \begin{Bmatrix} f_{b1}(y_{g1}) \\ f_{b2}(y_{g2}) \\ f_h(p) \end{Bmatrix} = \{F(t)\}. \tag{3a}$$

Here

$$\{F(t)\} = \{F\}_m + \{F(t)\}_i + \{F(t)\}_e = \begin{Bmatrix} -F_{b1} \\ F_{b2} \\ F_m \end{Bmatrix} + \begin{Bmatrix} 0 \\ 0 \\ F_{ah}\Omega_h^2 \end{Bmatrix} \sin(\Omega_h t + \phi_h) + \begin{Bmatrix} 0 \\ 0 \\ F_{aT} \end{Bmatrix} \sin(\Omega_T t + \phi_T), \tag{3b}$$

$$\zeta_{ii} = c_{bi}/2m_{gi}\omega_n, \qquad \zeta_{i3} = c_h/2m_{gi}\omega_n, \quad i = 1, 2, \qquad \zeta_{33} = c_h/2m_{c1}\omega_n, \tag{3c-e}$$

$$\kappa_{ii} = \omega_{bi}^2/\omega_n^2, \qquad \kappa_{i3} = m_{c1}/m_{gi}, \qquad F_{bi} = \bar{F}_{bi}/m_{gi}b_c\omega_n^2, \quad i = 1, 2, \tag{3f-h}$$

$$F_m = \bar{F}_m/m_{c1}b_c\omega_n^2, \qquad F_{ah} = \tilde{e}/b_c, \qquad F_{aT} = \tilde{F}_{aT}/m_{c1}b_c\omega_n^2, \tag{3i-k}$$

in which F_{bi} $(i = 1, 2)$ and F_m are the dimensionless components of the mean force vector $\{F\}_m$, and F_{aT} and F_{ah} pertain to the alternating external excitation $\{F(t)\}_e$ and internal excitation $\{F(t)\}_i$ force vectors, respectively.

2.4. MODELING OF NON-LINEARITIES

The non-linear displacement functions $f_{bi}(y_{gi})$, $i = 1, 2$ and $f_h(p)$ in equation (3a), which represent the bearing radial and gear mesh stiffnesses, respectively, should be defined explicitly before solving the non-linear equations. Here, $f_h(p)$ is defined as a clearance-type dead space function with a backlash $2b_h$ and linear time-invariant mesh stiffness of one, in the dimensionless form

$$f_h(p) = \begin{cases} p - b_h/b_c, & p > b_h/b_c \\ 0, & -b_h/b_c < p < b_h/b_c \\ p + b_h/b_c, & p < -b_h/b_c \end{cases}. \tag{4}$$

For the ith rolling element bearing, the radial force $\bar{F}_{yi}$ versus displacement $\bar{y}_{gi}$ relationship under the static loading condition is defined as [25–27]

$$\bar{F}_{yi}(\bar{y}_{gi}) = \begin{cases} k_{ti} \sum_{r=1}^{H} (\bar{y}_{gi} \cos\alpha_r - b_{bi})^n \cos\alpha_r, & \bar{y}_{gi} > b_{bi} \\ 0, & -b_{bi} < \bar{y}_{gi} < b_{bi} \\ -k_{ti} \sum_{r=1}^{H} (|\bar{y}_{gi}| \cos\alpha_r - b_{bi})^n \cos\alpha_r), & \bar{y}_{gi} < -b_{bi} \end{cases}, \tag{5}$$

where k_{ti} is the inner contact stiffness, α_r is the angular position of the rth rolling element in contact, $2b_{bi}$ is the radial clearance of the ith bearing, n is the power of the non-linear force displacement relationship ($n = 1{\cdot}5$ for ball bearings and $n = 10/9$ for roller bearings) and H is the total number of rolling elements in contact under loaded conditions. Now the dimensionless bearing displacement function $f_{bi}(y_{gi})$ of equation (3a) is obtained from equation (5) as

$$f_{bi}(y_{gi}) = \frac{\bar{F}_{vi}}{k_{ti} b_c^n} = \begin{Bmatrix} \sum_{r=1}^{H} (y_{gi} \cos \alpha_r - b_{bi}/b_c)^n \cos \alpha_r, & y_{gi} > b_{bi}/b_c \\ 0, & -b_{bi}/b_c < y_{gi} < b_{bi}/b_c \\ -\sum_{r=1}^{H} (|y_{gi}| \cos \alpha_r - b_{bi}/b_c)^n \cos \alpha_r, & y_{gi} < -b_{bi}/b_c \end{Bmatrix}. \quad (6)$$

In Figure 3 is shown the non-linear function $f_{gi}(y_{gi})$ for a roller bearing with $n = 10/9$, $k_t = 1 \times 10^8\ N/m^{10/9}$, the total number of rollers $Z = 15$ and $b_b = 0{\cdot}01$ mm. In Figure 3, one can note almost a linear relationship for large displacements, say $y_{gi} > 3b_{bi}/b_c$.

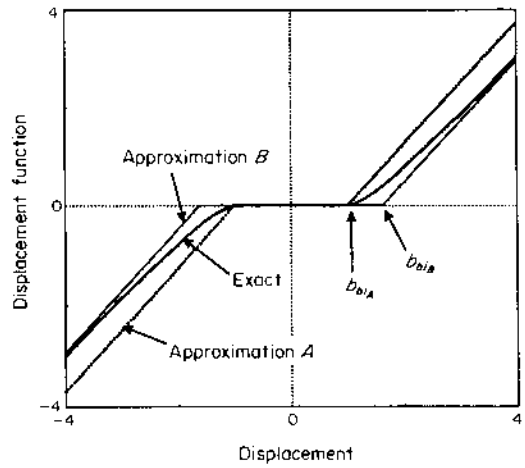

Figure 3. Exact and approximate bearing deflection functions.

Since the degree of non-linearity is not very significant, equation (6) can be approximated by a piecewise linear function, similar to $f_h(p)$ given by equation (4), in order to simplify the analysis considerably. In Figure 3 two linear approximations A and B beyond the clearance for $f_{bi}(y_{gi})$ in the form

$$f_{bi}(y_{gi}) = \begin{Bmatrix} y_{gi} - b_{bi}/b_c, & y_{gi} > b_{bi}/b_c \\ 0, & -b_{bi}/b_c < y_{gi} < b_{bi}/b_c \\ y_{gi} + b_{bi}/b_c, & y_{gi} < -b_{bi}/b_c \end{Bmatrix}. \quad (7)$$

are also illustrated. Note that both approximations A and B differ in clearances b_{bi_A} and b_{bi_B} but have the same slope as the exact bearing stiffness curve for $y_{gi} > 3b_{bi}/b_c$, $i = 1, 2$, which is unity in the dimensionless form. The validity of these approximations will be discussed later.

3. CORRESPONDING LINEAR MODEL

As a limiting case, equations of motion of the corresponding linear system are obtained by substituting $f_{bi}(y_{gi}) = y_{gi}$, for $i = 1$ and 2, and $f_h(p) = p$ in equation (3a), giving

$$\begin{bmatrix} 1 & 0 & 0 \\ 0 & 1 & 0 \\ -1 & 1 & 1 \end{bmatrix} \begin{Bmatrix} \ddot{y}_{g1}(t) \\ \ddot{y}_{g2}(t) \\ \ddot{p}(t) \end{Bmatrix} + 2 \begin{bmatrix} \zeta_{11} & 0 & \zeta_{13} \\ 0 & \zeta_{22} & -\zeta_{23} \\ 0 & 0 & \zeta_{33} \end{bmatrix} \begin{Bmatrix} \dot{y}_{g1}(t) \\ \dot{y}_{g2}(t) \\ \dot{p}(t) \end{Bmatrix} + \begin{bmatrix} \kappa_{11} & 0 & \kappa_{13} \\ 0 & \kappa_{22} & -\kappa_{23} \\ 0 & 0 & \kappa_{33} \end{bmatrix} \begin{Bmatrix} y_{g1}(t) \\ y_{g2}(t) \\ p(t) \end{Bmatrix} = \{F(t)\}, \tag{8a}$$

or in the matrix form, with $\{q(t)\}$ as the displacement vector,

$$[M]\{\ddot{q}(t)\} + [C]\{\dot{q}(t)\} + [K]\{q(t)\} = \{F(t)\}, \tag{8b}$$

where the mass $[M]$, damping $[C]$ and stiffness $[K]$ matrices are all positive definite. These matrices are asymmetric due to $\ddot{y}_{g1}$ and $\ddot{y}_{g2}$ terms in the last row of matrix equation (8a). For this linear system, the mean and alternating components of the motion can be separated by letting $y_{gi}(t) = y_{gim} + y_{gia}(t)$, $i = 1, 2$ and $p(t) = p_m + p_a(t)$. Hence, equation (8a) is rearranged in terms of the alternating motion as

$$[M]\{\ddot{q}_a(t)\} + [C]\{\dot{q}_a(t)\} + [K]\{q_a(t)\} = \{F(t)\}_i + \{F(t)\}_e. \tag{9}$$

The natural frequencies ω_r and the modes $\{\psi_r\}$ are calculated by considering the corresponding eigenvalue problem. The forced harmonic vibration response is then obtained by the modal expansion technique in the form

$$\{q_a(t)\} = \sum_{r=1}^{3} \frac{\{\psi_r\}\{\psi_r\}^T}{[(\omega_r^2 - \Omega_h^2) + j\Omega_h c_r]} F_{ah}\Omega_h^2 \sin(\Omega_h t + \phi_h) + \sum_{r=1}^{3} \frac{\{\psi_r\}\{\psi_r\}^T}{[(\omega_r^2 - \Omega_T^2) + j\Omega_T c_r]} F_{aT}\Omega_T^2 \sin(\Omega_T t + \phi_T), \qquad j = \sqrt{-1}, \tag{10a}$$

$$c_r = \frac{1}{\delta_{rs}} \{\psi^r\}^T [C]\{\psi^s\}, \qquad \delta_{rs} = \begin{cases} 1, & r = s \\ 0, & r \neq s \end{cases}. \tag{10b}$$

In Table 1 are shown the natural frequencies of the three-degree-of-freedom linear system given by equation (9), and the ones found by a finite element model [28], for

TABLE 1

Natural frequencies of the corresponding three degree of freedom (3-DOF) *linear model*

		$\hat{k} = k_{hi}/k_h$		
		1	5	10
ψ_r	ω_r	3-DOF/FEM†	3-DOF/FEM	3-DOF/FEM
First transverse-torsional coupled	ω_I	0·396/0·402	0·500/0·512	1·262/1·275
Purely transverse	ω_{II}	0·758/0·795	1·118/1·157	1·475/1·560
Second transverse-torsional coupled	ω_{III}	0·880/0·930	1·581/1·692	1·796/1·868

† Finite Element Method (FEM) from references [23, 28].

three different $\hat{k} = k_{hi}/k_h$ values with $m_{gi} = 1$ kg, $I_{gi} = 0{\cdot}0008$ kg/m^2, $d_{gi} = 0{\cdot}08$ m, $\zeta_{ii} = 0{\cdot}01$, $\zeta_{i3} = 0{\cdot}0125$, $\zeta_{33} = 0{\cdot}05$, $i = 1, 2$ and $k_h = 2 \times 10^8$ N/m. As is evident from Table 1, the three-degree-of-freedom and finite element models [23, 28] result in virtually the same natural frequencies. This demonstrates that the three-degree-of-freedom model is indeed suitable for the geared rotor–bearing system. The first, ψ_I, and third, ψ_{III}, natural modes are coupled transverse-torsional modes, while ψ_{II} is a purely transverse type [28]. The second natural mode ψ_{II} is not excited by $\bar{e}(\bar{t})$ in this particular case, since the gear ratio $v_g = d_{g2}/d_{g1}$ is one for a symmetric pair. Therefore only two peaks should exist in the frequency response spectrum which will be presented in section 5.

4. TWO-DEGREE-OF-FREEDOM SYSTEM STUDIES

4.1. EQUATIONS OF MOTION

As a first example, we reduce the three-degree-of-freedom transverse-torsional semi-definite model to a two-degree-of-freedom non-linear model. This is obtained by clamping one of the gear centers as shown in Figure 2(b): i.e., one of the transverse displacements is assumed to be zero, say $y_{g1} = 0$, which physically corresponds to a system with one gear $g1$ mounted on a rigid shaft which is supported by very stiff bearings while the other gear $g2$ is assembled with compliant lumped shaft and bearings. Equations of motion of the reduced order system are obtained from equation (3a) by letting $y_{g1} = 0$:

$$\begin{bmatrix} 1 & 0 \\ 1 & 1 \end{bmatrix} \begin{Bmatrix} \ddot{y}_{g2}(t) \\ \ddot{p}(t) \end{Bmatrix} + 2 \begin{bmatrix} \zeta_{22} & -\zeta_{23} \\ 0 & \zeta_{33} \end{bmatrix} \begin{Bmatrix} \dot{y}_{g2}(t) \\ \dot{p}(t) \end{Bmatrix} + \begin{bmatrix} \kappa_{22} & -\kappa_{23} \\ 0 & 1 \end{bmatrix} \begin{Bmatrix} f_{b2}(y_{g2}) \\ f_h(p) \end{Bmatrix} = \{F(t)\}. \quad (11)$$

The intent here is to simplify the physical system in order to investigate several key issues in depth. Specifically, the objectives are to (a) justify using approximate bearing models proposed in section 2.4 by comparing the frequency responses excited by $\bar{e}(\bar{t})$, (b) to show the applicability of the harmonic balance method (HBM) to solve non-linear system equations and compare its predictions with the results yielded by the digital simulation technique, (c) to study interactions between system non-linearities for both weakly and strongly coupled modes, and (d) to compare the steady state frequency response spectra due to internal static transmission error excitation $\{F(t)\}_i$ and external torque excitation $\{F(t)\}_e$.

4.2. SOLUTION

Both analytical and numerical solution techniques which we have used successfully for the spur gear pair problem [9] are employed again to solve equation (11). First, approximate analytical solutions are constructed by using the harmonic balance method [9, 22, 29] with only the bearing non-linearity and with no gear backlash: i.e. $b_h = 0$ or $f_h(p) = p$. For the harmonic excitation given by equation (3), one can assume

$$p(t) = p_m + p_a \sin(\Omega_h t + \phi_p), \qquad y_{g2}(t) = y_{g2m} + y_{g2a} \sin(\Omega_h t + \phi_{g2}), \quad (12a, b)$$

where subscripts m and a represent mean and alternating components of the steady state response, and ϕ_p and ϕ_{g2} are the phase angles. The non-linear bearing function is approximated as

$$f_{b2}(y_{g2}) = N_m y_{g2m} + N_a y_{g2a} \sin(\Omega_h t + \phi_{g2}), \quad (13)$$

where $N_m = N_m(y_{g2m}, y_{g2a})$ and $N_a = N_a(y_{g2m}, y_{g2a})$ are the describing functions which are given in reference [9]; these need to be defined for each impact regime (no impact, single-sided impact, double-sided impact). Governing frequency response equations are obtained by substituting equations (12) and (13) into equation (11) and equating the coefficients of like harmonics:

$$p_a = \frac{[\Lambda_1^2 + (2\zeta_{22}\Omega_h)^2]\Omega_h^2 F_{ah}}{\sqrt{\Lambda}}, \tag{14a}$$

$$\Lambda = (-\Omega_h^3\kappa_{23}\Lambda_1 + 4\Omega_h^4\zeta_{22}\zeta_{23} + \Lambda_2\Lambda_1^2 + 4\Omega_h^4\zeta_{22}^2\Lambda_2)^2 + (-2\Omega_h^3\zeta_{22}\kappa_{23} - 2\Omega_h^3\zeta_{23}\Lambda_1 + 2\Omega_h\zeta_{33}\Lambda_1^2 + 8\Omega_h^3\zeta_{22}^2\zeta_{33})^2, \tag{14b}$$

$$\Lambda_1 = \kappa_{22}N_a - \Omega_h^2, \qquad \Lambda_2 = 1 - \Omega_h^2, \qquad p_m = F_m, \tag{14c-e}$$

$$y_{g2a} = \left[\frac{\kappa_{23}^2 + (2\Omega_h\zeta_{23})^2}{(\kappa_{23}\Lambda_1 - 4\Omega_h^2\zeta_{22}\zeta_{23})^2 + (2\Omega_h\zeta_{22}\kappa_{23} + 2\Omega_h\zeta_{23}\Lambda_1)^2}\right]^{1/2}, \qquad y_{g2m} = \frac{F_{b2} + \kappa_{23}p_m}{\kappa_{22}N_m}. \tag{14f, g}$$

The overall frequency response is obtained by solving equation (14) numerically for each impact regime separately, as in our earlier study [9].

Second, the digital simulation technique is used to solve equation (11) for no gear backlash. A fifth-sixth order variable step size Runge-Kutta numerical integration algorithm [30], which has already been employed successfully [9] in solving similar problems, is used here. Frequency response spectra as obtained by using the harmonic balance method and digital simulation, respectively, are compared in Figure 4. Although

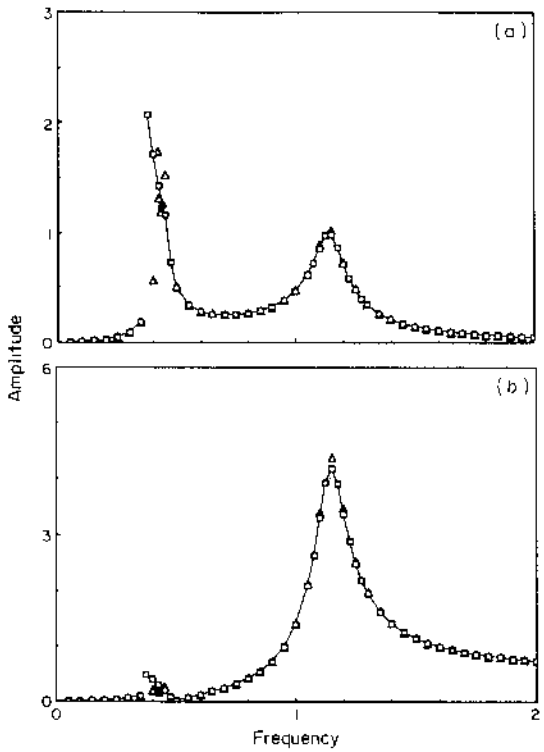

Figure 4. Comparison of harmonic balance method (Λ) and digital simulation technique (—└—); $F_m = 1{\cdot}0$, $F_{ah} = 0{\cdot}5$, $F_{b2} = 0$, $b_h = 0$, $b_{h2} = b_c$, $\zeta_{33} = 0{\cdot}05$, $\zeta_{23} = 0{\cdot}0125$, $\zeta_{22} = 0{\cdot}01$, $\hat{k} = 1$; (a) y_{g2a} versus Ω_h; (b) p_a versus Ω_h.

both methods are in a very close agreement for the case considered in Figure 4, one should be aware of the following: (i) several problems may exist in the application of the numerical integration method to the clearance type problems, and hence caution must be exercised [9]; (ii) the harmonic balance method is incapable of predicting chaotic and subharmonic responses. Accordingly, for further analysis, only the digital simulation technique is to be used.

4.3. VALIDATION OF NON-LINEAR BEARING MODEL

One can now examine the validity of the two approximations for $f_{bi}(y_{gi})$, as suggested in section 2.4 and shown in Figure 3, by assuming $b_h = 0$ and $F_{aT} = 0$. Equation (11) has been solved by using the digital simulation technique, given $F_m = 1{\cdot}0$, $F_{ah} = 0{\cdot}05$, $F_{b2} = 0$, $\zeta_{22} = 0{\cdot}01$, $\zeta_{33} = 0{\cdot}05$, $\zeta_{23} = 0{\cdot}0125$ and $\kappa_{22} = \kappa_{23} = 0{\cdot}25$, for three bearing models (exact, approximation A, $b_{b2_A} = b_{b2} = b_c$; approximation B, $b_{b2_B} = 1{\cdot}63\ b_{b2} = 1{\cdot}63\ b_c$). In Figures 5(a) and 5(b) y_{g2a} versus Ω_h and $\dot{y}_a$ versus Ω_h spectra are compared for all three bearing models. Both approximations give results in a very close agreement with the exact bearing model results over the entire frequency range. The frequency and the amplitude of the jump at the first peak is predicted accurately by both approximate models. Hence one can conclude that the approximate piecewise linear model can be used for a bearing without losing any accuracy, and that the dynamic behavior is not sensitive to the minor variations in bearing clearances b_{bi}.

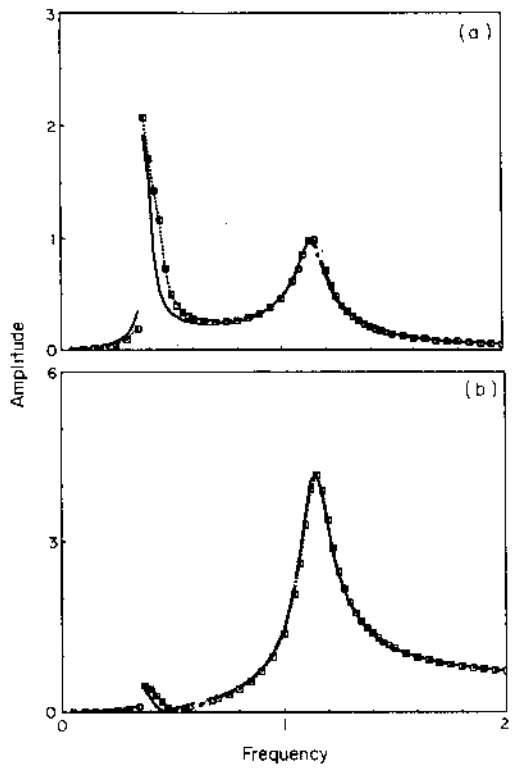

Figure 5. Comparison of frequency responses obtained by using the exact (——) and approximate (· · · · A and □ B) bearing displacement functions given in Figure 3; $F_m = 1{\cdot}0$, $F_{ah} = 0{\cdot}5$, $F_{b2} = 0$, $b_h = 0$, $b_{b2} = b_c$, $\zeta_{33} = 0{\cdot}05$, $\zeta_{23} = 0{\cdot}0125$, $\zeta_{22} = 0{\cdot}01$, $\hat{k} = 1$; (a) y_{g2a} versus Ω_h; (b) p_a versus Ω_h.

4.4. NON-LINEAR MODAL INTERACTIONS

Although both natural modes of the corresponding linear model are transverse-torsional coupled modes, the first mode ψ_1 is more dependent on transverse vibrations than the second [23]. Accordingly, it is expected that bearing non-linearities should affect the first peak directly while gear backlash should dominate the second peak in Figure 4. The validity of this claim depends on the nature of non-linearities and system parameter values, as illustrated below.

First, a set of parameters was selected so that the natural frequencies ω_I and ω_{II} of the corresponding linear system are far away from each other: $\omega_I = 0{\cdot}437$ and $\omega_{II} = 1{\cdot}144$ for $\kappa_{22} = 0{\cdot}25$, $\kappa_{23} = 0{\cdot}25$, $\zeta_{22} = 0{\cdot}01$, $\zeta_{23} = 0{\cdot}0125$, and $\zeta_{33} = 0{\cdot}05$. Frequency response characteristics of the system with a forcing function $F_m = 1{\cdot}0$ and $F_{ah} = 0{\cdot}5$ were evaluated for the following three cases: (a) no gear backlash, $b_h = 0$, non-linear bearing, $b_{b2} = b_c$; (b) gear backlash, $b_h = 10b_c$, linear bearing, $b_{b2} = 0$; (c) gear backlash and non-linear bearing with $b_h = 10\ b_{b2} = 10b_c$. In the last two cases, gear backlash was taken to be 10 times the bearing clearance as this is a typical order of magnitude value for many geared rotor systems supported by roller bearings. In Figures 6 and 7 are shown the frequency responses, y_{g2a} versus Ω_h and p_a versus Ω_h respectively, for all three cases given above; also superimposed is the linear frequency response curve for comparison purposes. As shown in Figures 6(a) and 7(a), a jump discontinuity is observed at the first peak only for case (a). In the case with only gear backlash non-linearity, a jump is seen at the second peak while the first peak is continuous as shown in Figures 6(b) and 7(b); this supports the claim of torsional mode dominance of the second peak. Finally, when both non-linearities are included simultaneously, both peaks become non-linear, as shown in Figures 6(c)

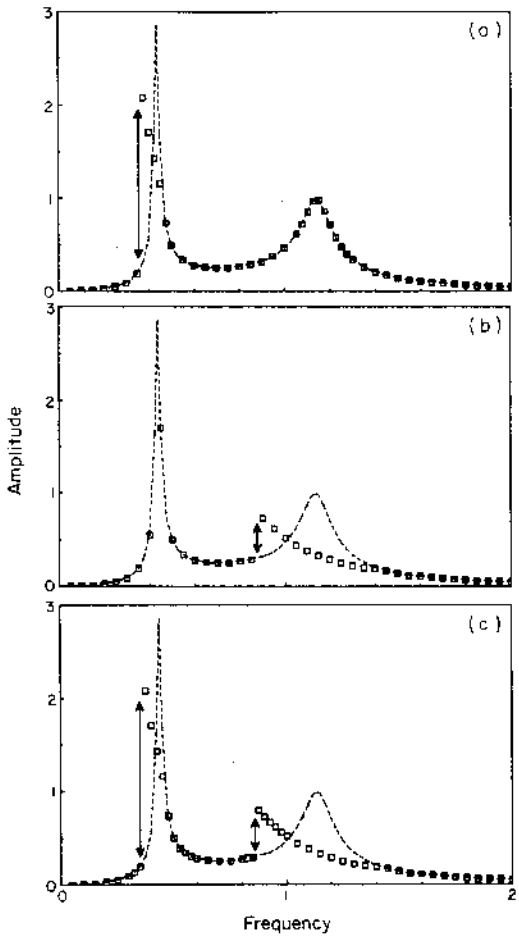

Figure 6. y_{g2a} versus Ω_h plots for the case of uncoupled modes; (a) no backlash, non-linear bearings; (b) backlash, linear bearings; (c) backlash, non-linear bearings; – – –, corresponding linear response.

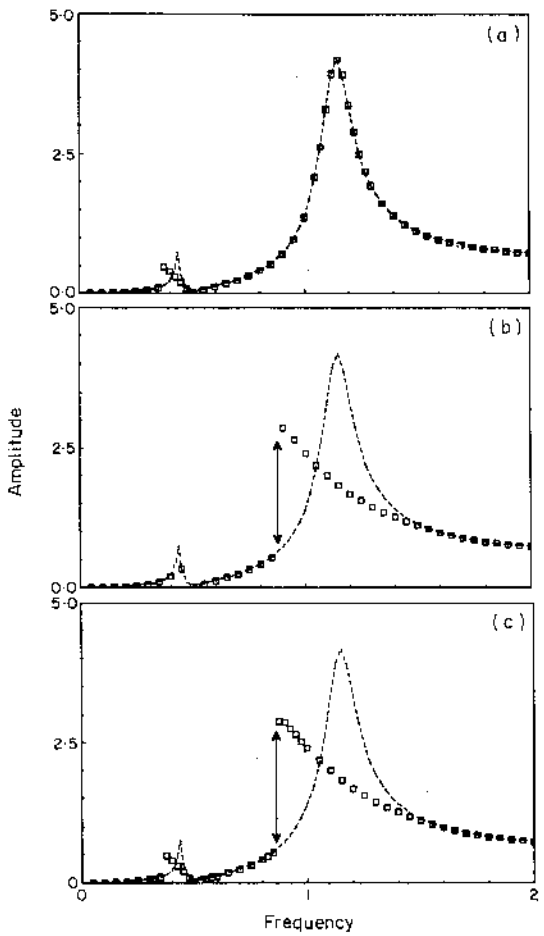

Figure 7. p_a versus Ω_h plots for the case of uncoupled modes; (a) no backlash, non-linear bearings; (b) backlash, linear bearings, (c) backlash, non-linear bearings; - - -, corresponding linear response.

and 7(c). For such a system, natural modes are essentially "uncoupled" and the interactions between component non-linearities are negligible. In summary, for case (a) of Figures 6(a) and 7(a), a linear model can be used to predict the frequency response beyond ω_I, say $\Omega_h > 0{\cdot}6$. Similarly, a linear model could be suitable for case (b) for $\Omega_h < 0{\cdot}8$ as shown in Figures 6(b) and 7(c). But for case (c), a linear model is suitable only far away from the resonances.

Second, a dataset was chosen, say $\kappa_{22} = 0{\cdot}64$, $\kappa_{23} = 0{\cdot}10$, $\zeta_{22} = 0{\cdot}01$, $\zeta_{23} = 0{\cdot}0125$, and $\zeta_{33} = 0{\cdot}05$, such that two natural frequencies for the corresponding linear system are brought closer to each other: $\omega_I = 0{\cdot}720$, $\omega_{II} = 1{\cdot}101$. The same cases (a), (b) and (c) were considered and the frequency responses for $F_m = 2{\cdot}0$ and $F_{ah} = 0{\cdot}5$ were compared, as shown in Figures 8 and 9. Here, each non-linearity affects both modes, resulting in jumps at each peak. Therefore, for this set of parameters, modes are considered to be "coupled" because of dynamic interactions. Accordingly, both non-linearities must be included simultaneously in the dynamic model.

4.5. INTERNAL VERSUS EXTERNAL EXCITATION

Next one can consider applying only one type of excitation at a time and compare frequency response characteristics of the system due to sinusoidal excitations $\{F(t)\}_i$ and

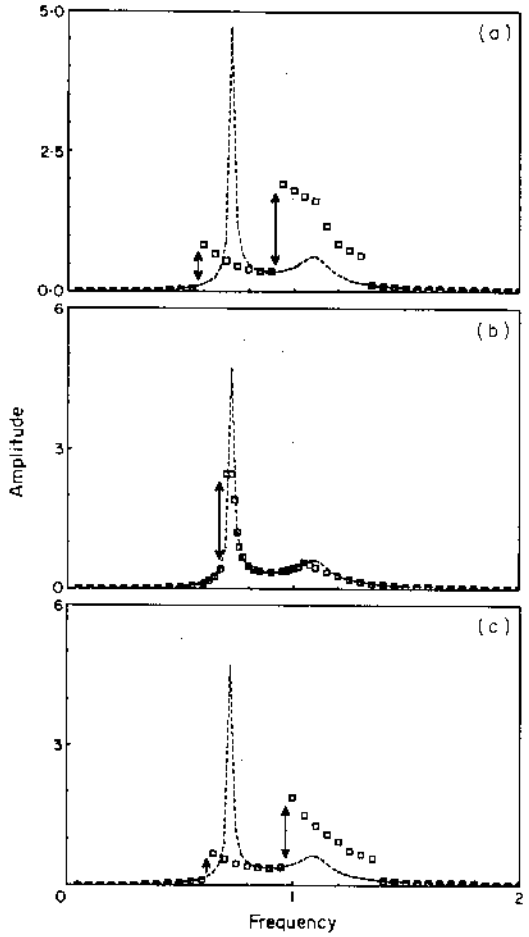

Figure 8. y_{g2a} versus Ω_h plots for the case of coupled modes; (a) no backlash, non-linear bearings; (b) backlash, linear bearings; (c) backlash, non-linear bearings; - - -, corresponding linear response.

$\{F(t)\}_e$ in equation (3a). Here, only the bearing non-linearity will be considered, with no tooth separation: $b_h = 0$. In the case of internal excitation, the amplitude of the alternating component is dependent on Ω_h^2. Conversely, the amplitude of the alternating external force is frequency independent. Therefore, for a constant force ratio F_{ai}/F_m, $i = h, T$, the overall amplitude ratio $\Omega_h^2 F_{ah}/F_m$ for internal excitation varies with excitation frequency, whereas the overall amplitude ratio F_{aT}/F_m for external excitation remains constant, a behavior similar to that of the single-degree-of-freedom model [9].

In Figures 10(a) and 10(b) are shown comparisons of y_{g2a} versus Ω and p_a versus Ω spectra for $\Omega_t = \Omega_h = \Omega$, $F_m = 1{\cdot}0$, $F_{aT} = F_{ah} = 0{\cdot}5$, $F_{b2} = 0$, $\zeta_{22} = 0{\cdot}01$, $\zeta_{23} = 0{\cdot}0125$, $\zeta_{33} = 0{\cdot}05$ and $\kappa_{22} = \kappa_{23} = 0{\cdot}25$. As shown in Figures 10(a) and 10(b), both excitations yield the same values at $\Omega = 1{\cdot}0$ since $F_m/F_{aT} = F_m/\Omega^2 F_{ah}$ at $\Omega = 1{\cdot}0$. For $\Omega > 1$ the internal excitation gives larger amplitudes than the external excitation, but the converse is true for $\Omega < 1$. Another important difference is that, for increasing Ω, there are two jumps (a jump-up from the no-impact regime to the double-sided impact regime at $\Omega = 0{\cdot}3$ and a jump-down from the double-sided to the single-sided impact regimes at $\Omega = 0{\cdot}4$) for the external excitation; but the double-sided impact regime is not seen in the internal excitation case and only one jump from the no-impact to the single-sided impact is found at $\Omega = 0{\cdot}35$.

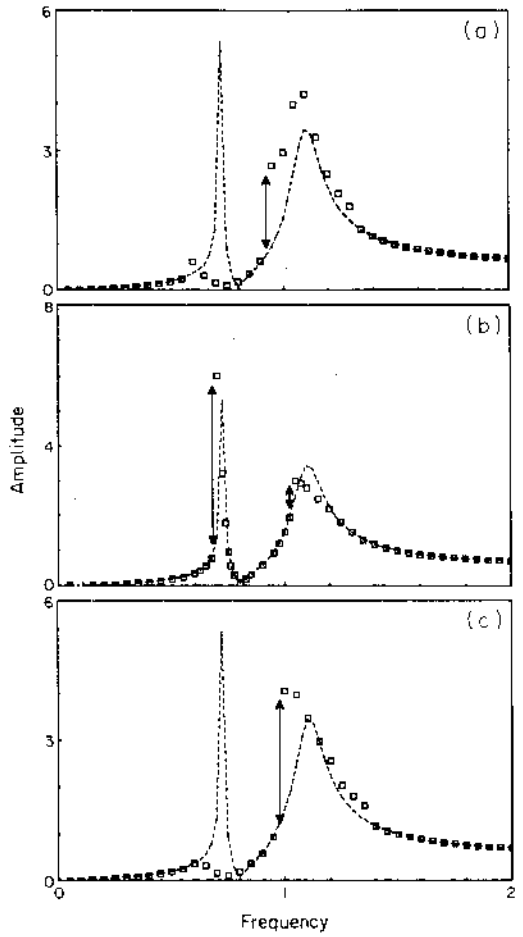

Figure 9. p_a versus Ω_h plots for the case of coupled modes; (a) no backlash, non-linear bearings; (b) backlash, linear bearings; (c) backlash, non-linear bearings; – – –, corresponding linear response.

5. THREE-DEGREE-OF-FREEDOM SYSTEM STUDIES

5.1. CLASSIFICATION OF STEADY STATE SOLUTIONS

The steady state response results excited by an internal force $\{F(t)\}_i$ at each frequency Ω_h have been categorized into the following five groups: (i) harmonic or nearly harmonic solution at the same period $t_p = 2\pi/\Omega_h$ as that of the forcing function (period-one); (ii) non-harmonic period-one solution; (iii) subharmonic solution with period nt_p, $n > 1$; (iv) quasi-periodic solution; (v) chaotic solution (non-periodic, $n \to \infty$). The solution classification criteria are based on time histories, phase plane plots, Poincaré maps and Fourier spectra [31–36]. In Figures 11–15 different types of steady state solutions obtained from the three-degree-of-freedom non-linear model of Figure 2(a) are illustrated. As shown in Figure 11, period-one, non-harmonic solutions have a non-circular (non-elliptic) phase plane plot and repeat themselves at t_p. In Figure 12 are shown the time histories, phase plane plots and Poincaré maps for a $2t_p$ subharmonic solution. In this case, the Poincaré map consists of two discrete points. Similarly, the $6t_p$ (ultra)subharmonic response has six points on the Poincaré map, as shown in Figure 13. In Figure 14 a typical quasi-periodic response (combination oscillations) is illustrated which consists of two or

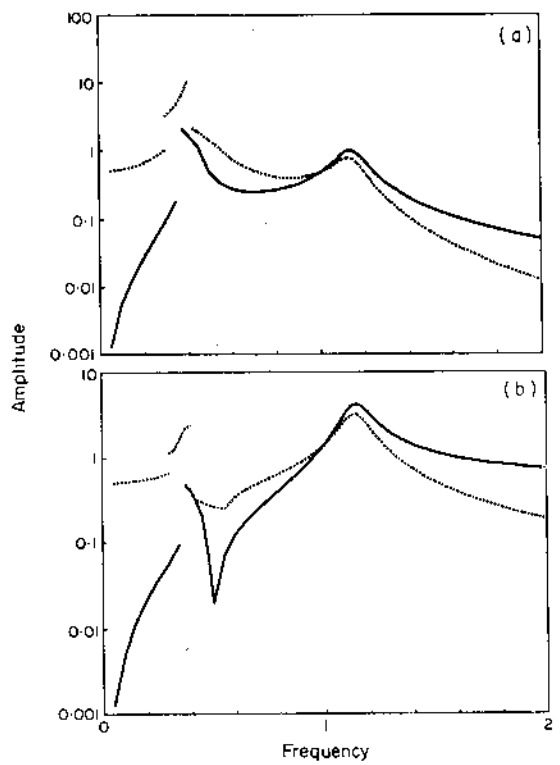

Figure 10. Comparison of frequency responses due to internal static transmission error (——) and external torque excitation (· · · ·); $F_m = 1{\cdot}0$, $F_{ah} = 0{\cdot}5$, $F_{h2} = 0$, $b_h = 0$, $b_{h2} = b_c$, $\zeta_{33} = 0{\cdot}05$, $\zeta_{23} = 0{\cdot}0125$, $\zeta_{22} = 0{\cdot}01$, $\hat{k} = 1$; (a) y_{g2a} versus Ω_h; (b) p_a versus Ω_h.

more "incommensurate" frequencies [31, 32]. Quasi-periodic solutions result in closed orbits on the Poincaré map, as shown in Figure 14(c). The chaotic responses which are defined by a non-periodic time history and as many points as the number of cycles considered in the analysis on the Poincaré map are illustrated in Figure 15. In Figures 16(a)–(e) are shown the FFT spectra corresponding to the time histories given in Figures 11–15. For the period-one non-harmonic solution of Figure 11, the corresponding spectrum has peaks at $m\omega$, where ω is the fundamental frequency and m is a positive integer, as shown in Figure 16(a). The nt_p subharmonic solutions contain peaks at the frequencies $m\omega/n$. For instance, spectra of the $2t_p$ and $6t_p$ solutions of Figures 12 and 13 have peaks at frequencies $m\omega/2$ and $m\omega/6$ respectively in Figures 16(b) and (c). The quasi-periodic solution of Figure 14 consists of two fundamental frequencies ω_1 and ω_2 at a ratio ω_1/ω_2 (an irrational number ≈ 8) and there are peaks at the combination frequencies $m\omega_1 + r\omega_2$, $m, r = 0, \pm 1, \pm 2, \ldots$. Finally, a characteristic broad band spectrum is obtained in Figure 16(e) when the solution as shown in Figure 15 is chaotic.

5.2. ROUTES TO CHAOS

Earlier we had investigated the effect of mean load F_m and damping ζ on the chaotic response of a gear pair [9]. It has been shown that chaos typically exists in lightly damped and lightly loaded gear pairs. Now, two different routes to chaos for the three-degree-of-freedom system are illustrated.

(a) *Period-doubling route to chaos.* This consists of a sequence of bifurcations of the periodic response to another periodic response with twice the period of the original

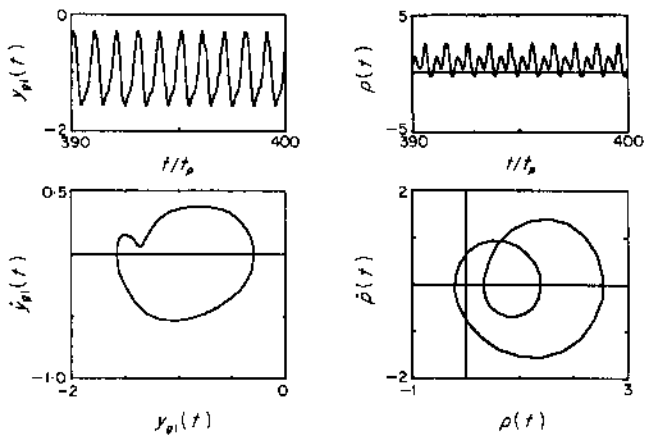

Figure 11. A non-harmonic period-one response; $F_m = 1{\cdot}0$, $F_{ah} = 0{\cdot}5$, $F_{bi} = 0$, $b_h = 0$, $b_{h2} = b_c$, $\zeta_{33} = 0{\cdot}05$, $\zeta_{13} = \zeta_{23} = 0{\cdot}0125$, $\zeta_{11} = \zeta_{22} = 0{\cdot}01$, $\hat{k} = 5$, $\Omega_h = 0{\cdot}6$; (a) time histories; (b) phase plane plots.

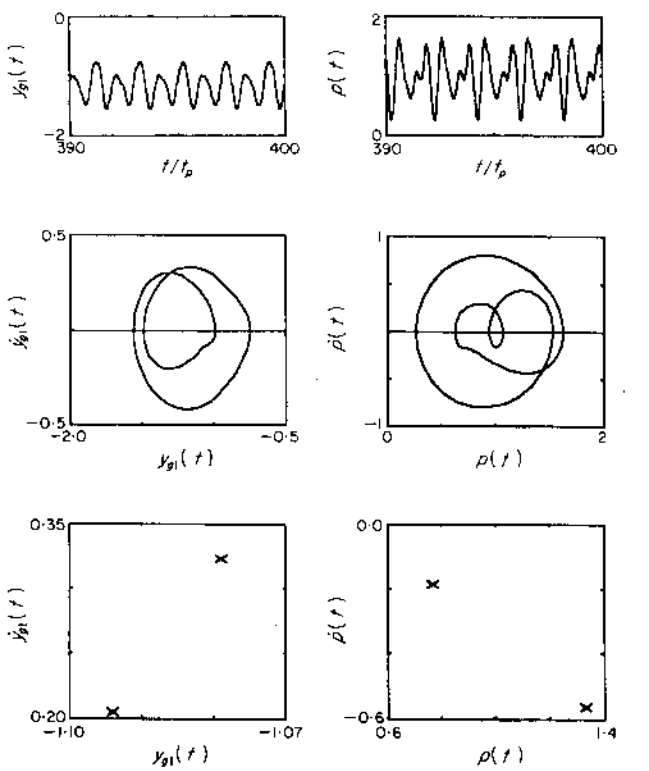

Figure 12. A period-two subharmonic response; $F_m = 1{\cdot}0$, $F_{ah} = 0{\cdot}5$, $F_{bi} = 0$, $b_h = 0$, $b_{h2} = b_c$, $\zeta_{33} = 0{\cdot}05$, $\zeta_{13} = \zeta_{23} = 0{\cdot}0125$, $\zeta_{11} = \zeta_{22} = 0{\cdot}01$, $\hat{k} = 5$, $\Omega_h = 0{\cdot}85$.

response due to a change in one of the system parameters [31, 33–35]. This is demonstrated in Figure 17 with a change in excitation frequency Ω_h given $F_m = 0{\cdot}1$, $F_{ah} = 0{\cdot}05$, $F_{bi} = 0$, $i = 1, 2$, $\zeta_{11} = \zeta_{22} = 0{\cdot}01$, $\zeta_{13} = \zeta_{23} = 0{\cdot}0125$, $\zeta_{33} = 0{\cdot}05$, $\kappa_{11} = \kappa_{22} = 1{\cdot}25$, $\kappa_{13} = \kappa_{23} = 0{\cdot}25$, $b_c = b_h$ and $b_{bi} = 0$, $i = 1, 2$. At $\Omega_h = 1{\cdot}500$, with zero initial conditions, one can note a t_p harmonic solution in Figure 17(a). This t_p solution bifurcates to the $2t_p$ subharmonic solution in Figure 17(b) when Ω_h is reduced to $\Omega_h = 1{\cdot}48$. Furthermore, at $\Omega_h = 1{\cdot}44$ a

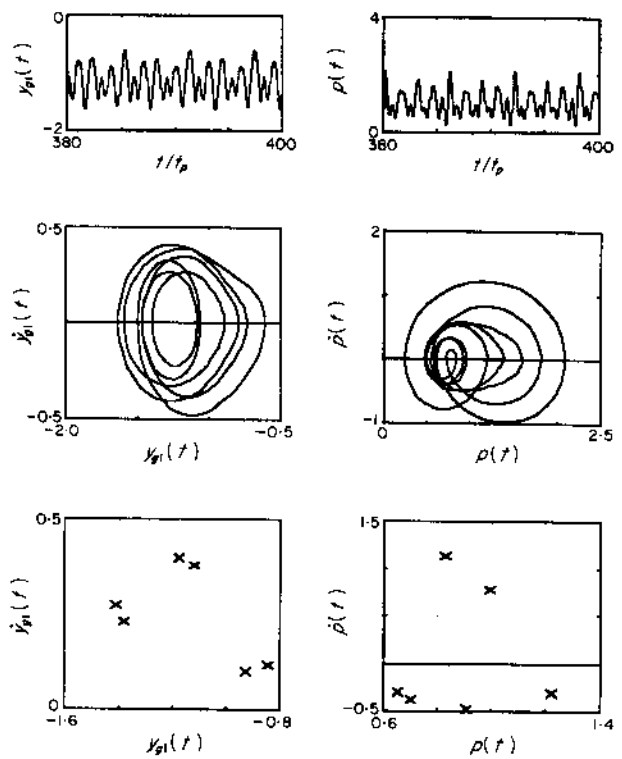

Figure 13. A period-six (ultra)subharmonic response; $F_m = 1{\cdot}0$, $F_{ah} = 0{\cdot}5$, $F_{b2} = 0$, $b_h = 0$, $b_{h2} = b_c$, $\zeta_{33} = 0{\cdot}05$, $\zeta_{13} = \zeta_{23} = 0{\cdot}0125$, $\zeta_{11} = \zeta_{22} = 0{\cdot}01$, $\hat{k} = 5$, $\Omega_h = 1{\cdot}0$.

$4t_p$ solution is obtained which is further transformed to a $8t_p$ response at $\Omega_h = 1{\cdot}402$ as shown in Figures 17(c) and (d), respectively. At $\Omega_h = 1{\cdot}4$, however, the steady state solution becomes chaotic, as evident from Figure 17(e). Also note from spectra of Figures 17(a)–(e) that the single peak spectrum is transformed to a broadband spectrum corresponding to chaos through period-doubling.

(b) *Quasi-periodic route to chaos.* In this case, instead of going through the period doubling, the response undergoes a sequence of Hopf bifurcations with a change in a system parameter. First a quasi-periodic response and finally a chaotic response are obtained [31, 36]; such a route to chaos is shown in Figure 18. $3t_p$ solution at $\Omega_h = 1{\cdot}1$ bifurcates to a quasi-periodic solution when Ω_h is increased to 1·2, as shown in Figure 18(a) and (b). A further increase in Ω_h to 1·3 yields a deformed closed orbit Poincaré map, as shown in Figure 18(c). It is then transformed to a chaotic strange attractor at $\Omega_h = 1{\cdot}4$ in Figure 18(d). Similar observations are evident from the Fourier spectra shown in Figures 18(b)–(d); the spectrum consists of combination frequencies for the quasi-periodic solution, but if finally changes to a broadband spectrum characteristic of chaos.

5.3. PARAMETRIC STUDIES

The three-degree-of-freedom non-linear model of Figure 2(a) has been used to study the effect of several system parameters such as the stiffness ratio, $\hat{k} = k_{bi}/k_h$, $i = 1, 2$, the radial bearing preload to mean load ratio, F_{bi}/F_m, $i = 1, 2$, and the alternating load to mean load ratio F_{ah}/F_m on the non-linear dynamic behavior. A geared rotor–bearing system of one-to-one gear ratio ($v_g = 1$) with $m_{gi} = 1$ kg, $I_{gi} = 0{\cdot}0008$ kg/m^2, $d_{gi} = 0{\cdot}08$ m, $i = 1, 2$, and mesh stiffness $k_h = 2 \times 10^8$ N/m was selected. Five percent mesh damping

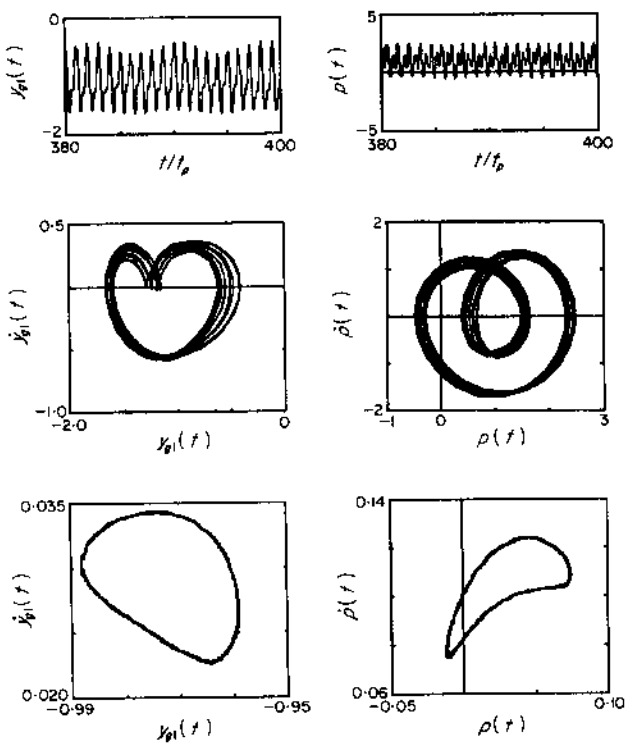

Figure 14. A quasi-periodic response; $F_m = 1{\cdot}0$, $F_{ah} = 0{\cdot}5$, $F_{b2} = 0$, $b_h = 0$, $b_{h2} = b_c$, $\zeta_{33} = 0{\cdot}05$, $\zeta_{13} = \zeta_{23} = 0{\cdot}0125$, $\zeta_{11} = \zeta_{22} = 0{\cdot}01$, $\hat{k} = 5$, $\Omega_h = 0{\cdot}65$.

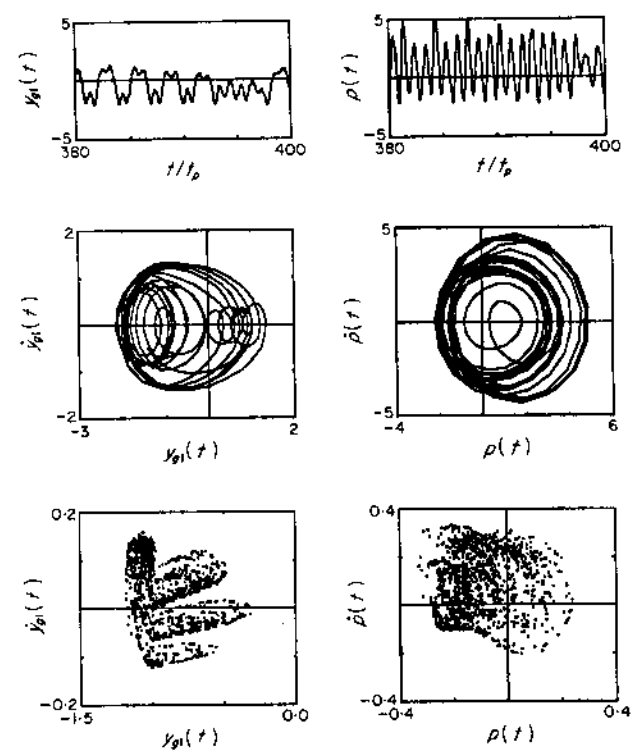

Figure 15. A chaotic response; $F_m = 1{\cdot}0$, $F_{ah} = 0{\cdot}5$, $F_{b2} = 0$, $b_h = 0$, $b_{h2} = b_c$, $\zeta_{33} = 0{\cdot}05$, $\zeta_{13} = \zeta_{23} = 0{\cdot}0125$, $\zeta_{11} = \zeta_{22} = 0{\cdot}01$, $\hat{k} = 5$, $\Omega_h = 0{\cdot}85$.

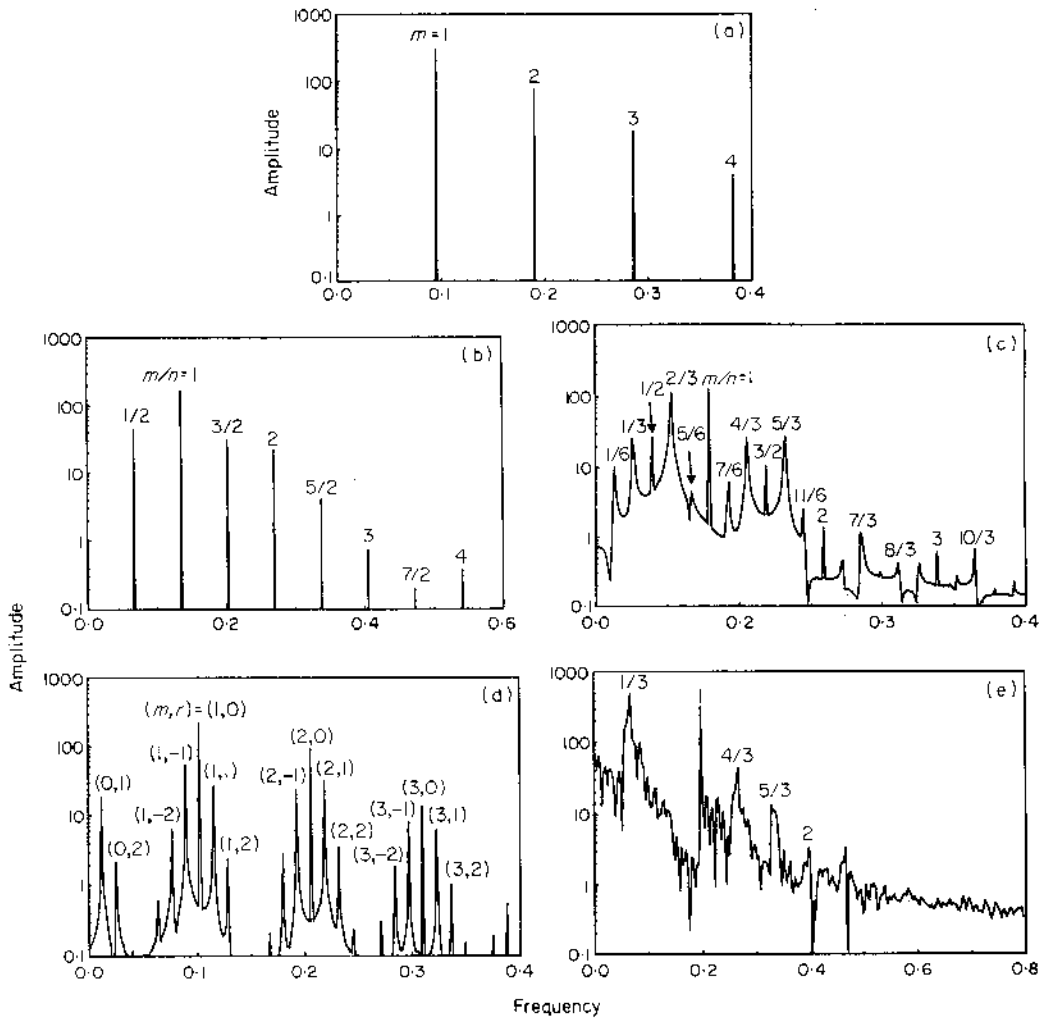

Figure 16. FFT spectra of $y_{g2}(t)$ for the responses given in Figures 11–15; (a) period-one; (b) period-two; (c) period-six; (d) quasi-linear; (e) chaos.

and one percent bearing damping values, which are somewhat realistic [37, 38], were used: i.e., $\zeta_{11}=\zeta_{22}=0{\cdot}01$, $\zeta_{13}=\zeta_{23}=0{\cdot}0125$ and $\zeta_{33}=0{\cdot}05$. Both non-linearities were considered separately in this parametric study. The case when both bearing non-linearities and backlash exist simultaneously was not considered here, as it has already been examined in section 4 by using the two-degree-of-freedom model.

5.3.1. *Gear backlash, linear bearings*

For the non-linear model of Figure 2(a) with linear bearings ($b_{bi}=0$), b_h is used as the characteristic length b_c. In Figures 19(a) and 20(a) shown $y_{g1a}(\Omega_h)$ and $p_a(\Omega_h)$ spectra for the soft bearings ($\hat{k}=1$) with $F_m=0{\cdot}1$ and $F_{ah}/F_m=0{\cdot}5$. Here the y_{g2a} spectrum is not included since $y_{g1a}=y_{g2a}(y_{g1}(t)=-y_{g2}(t))$ for a one-to-one gear ratio. As is evident from Figures 19(a) and 20(a), y_{g1a} at the first peak is larger than that seen at the second peak. Conversely, p_a is much lower at the first peak, implying that the first mode is dominated by the transverse vibrations whereas the second mode is dictated by the torsional vibrations for soft bearings. This corresponds to a large dynamic bearing force

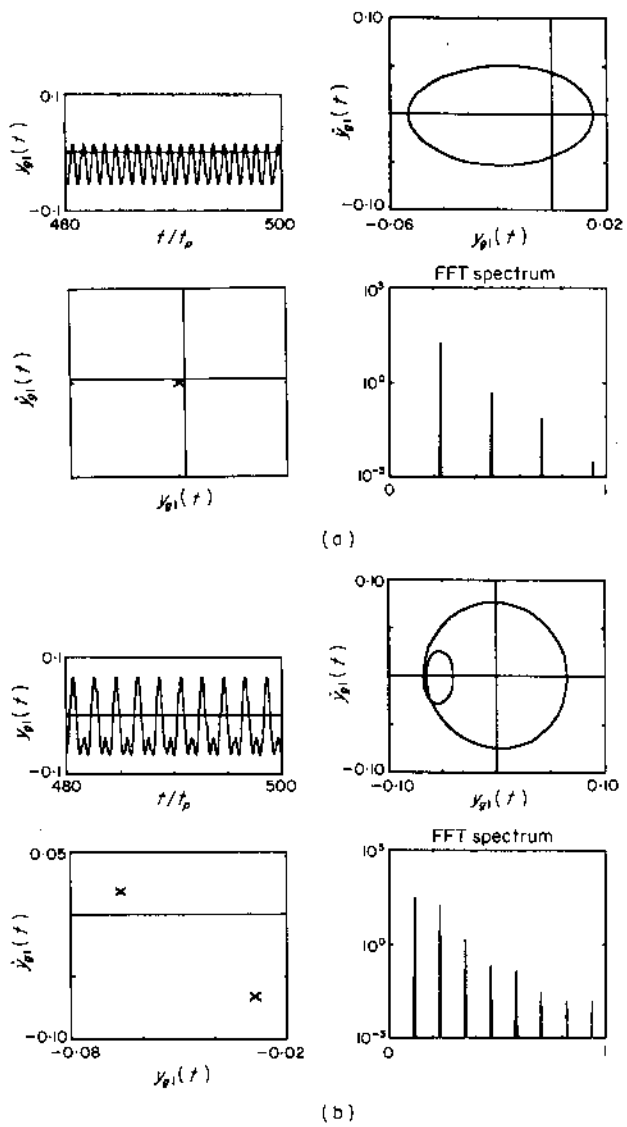

Figure 17. Period-doubling route to chaos; $F_m = 0{\cdot}1$, $F_{ah} = 0{\cdot}05$, $F_{b2} = 0$, $b_h = b_c$, $b_{b2} = 0$, $\zeta_{33} = 0{\cdot}05$, $\zeta_{13} = \zeta_{23} = 0{\cdot}0125$, $\zeta_{11} = \zeta_{22} = 0{\cdot}01$, $\hat{k} = 5$; (a) period-one, $\Omega_h = 1{\cdot}5$; (b) period-two, $\Omega_h = 1{\cdot}48$; (c) period-four, $\Omega_h = 1{\cdot}44$, (d) period-eight, $\Omega_h = 1{\cdot}402$; (e) chaos, $\Omega_h = 1{\cdot}4$.

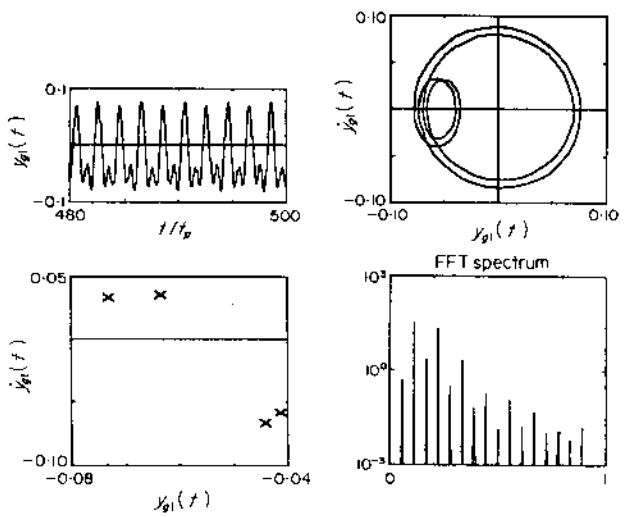

(c)

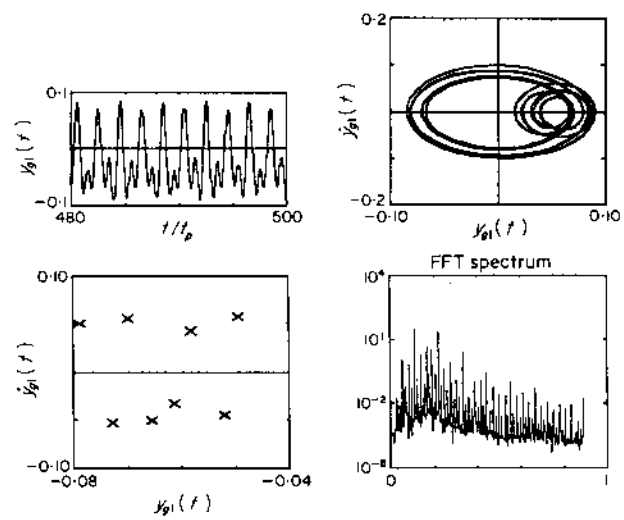

(d)

Figure 17—*continued.*

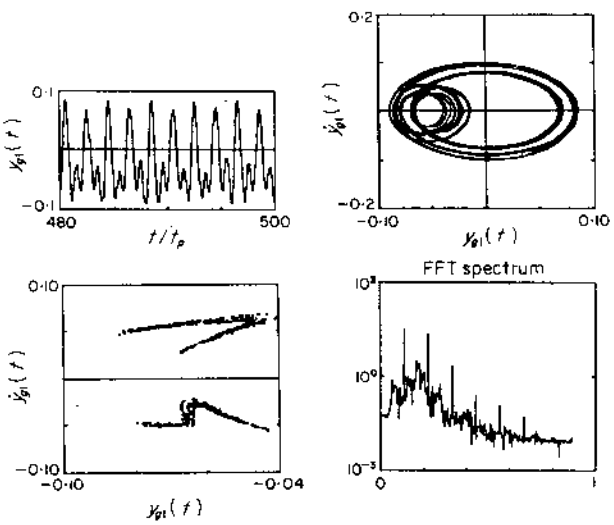

(e)

Figure 17—*continued.*

$F_{dbi} \approx k_{bi} y_{gi}$, but a small dynamic transmission error ($p(t) + e(t)$) around the first natural frequency. A jump phenomenon is observed only at the second peak, which is governed by the gear mesh where the excitation $e(t)$ is applied. This indicates that for $\hat{k} = 1$ the modes are weakly coupled. Accordingly, the gear mesh non-linearity, which forces the second peak to be non-linear, does not affect the linear characteristics of the first peak. However, the modal coupling becomes stronger with an increase in $\hat{k}$, as is evident from the jumps seen at both peaks in Figures 19(b) and 20(b) for $\hat{k} = 5$ and Figures 19(c) and 20(c) for $\hat{k} = 10$. Torsional vibrations start to dominate the first mode, and the second peak shifts upward and it may eventually move out of the operational speed range. Therefore, for a large $\hat{k}$ value associated with stiff shafts and bearings, a single degree of freedom torsional model as used earlier by us [9] should be sufficient. Another effect of a large $\hat{k}$ is that the nt_p subharmonic solutions replace some of the harmonic solutions as shown in Figures 19(b), (c) and 20(b), (c).

In Figures 21(a), 22(a) and 21(b), 22(b) the effects of the load ratio for $F_{ah}/F_m = 0{\cdot}5$ and 1, respectively, are shown, with $F_m = 0{\cdot}1$ and $\hat{k} = 1$. The frequency response is well defined and dominated by the harmonic solutions for $F_{ah}/F_m = 0{\cdot}5$. However, when F_{ah}/F_m is increased to 1, the region beyond $\Omega_h = 1{\cdot}0$ becomes strongly non-linear, consisting of subharmonic, quasi-periodic or chaotic responses. This was also seen for the gear pair model [9].

5.3.2. *No gear backlash, non-linear bearings*

Now consider the same system with $b_h = 0$ and non-linear bearings described by the approximate model given in section 2.4. Results are presented for both roller and ball bearings separately, since the radial clearance in a ball bearing is much smaller than that typically found in a roller bearing with the same inner and outer race diameters; say $b_{bi_{roller}} \approx 10\, b_{bi_{ball}}$. For each case, b_{bi} is used as the characteristic length b_c.

In Figures 23 and 24 are shown the steady state frequency response plots for the roller bearings of $b_{bi} = 0{\cdot}01$ mm ($i = 1, 2$), for three different $\hat{k} = k_{bi}/k_h$ values. As shown in Figures 23(a) and 24(a), for soft bearings ($\hat{k} = 1$), two modes of interest are weakly coupled, and therefore the jump phenomenon is seen only at the first peak which is

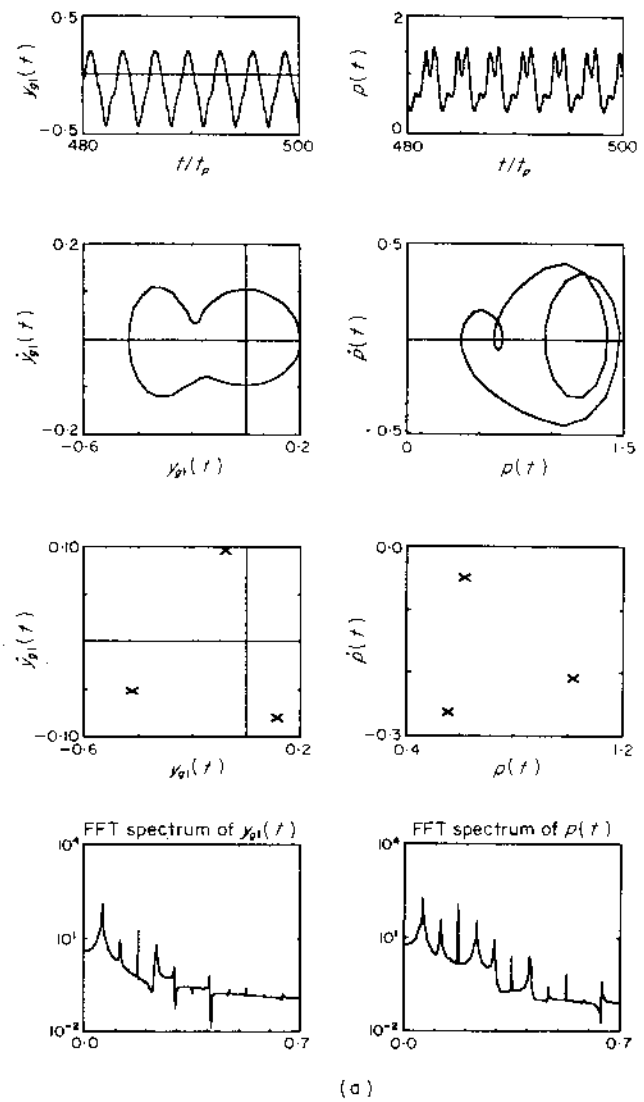

(a)

Figure 18. Quasi-periodic route to chaos; $F_m = 0{\cdot}1$, $F_{ah} = 0{\cdot}05$, $F_{b2} = 0$, $b_h = b_c = 0{\cdot}1$, $b_{b2} = 0$, $\zeta_{33} = 0{\cdot}05$, $\zeta_{13} = \zeta_{23} = 0{\cdot}0125$, $\zeta_{11} = \zeta_{22} = 0{\cdot}01$, $\hat{k} = 1$; (a) period three, $\Omega_h = 1{\cdot}1$; (b) quasi-periodic, $\Omega_h = 1{\cdot}2$; (c) transition from quasi-periodic to chaotic response, $\Omega_h = 1{\cdot}3$; (d) chaos, $\Omega_h = 1{\cdot}4$.

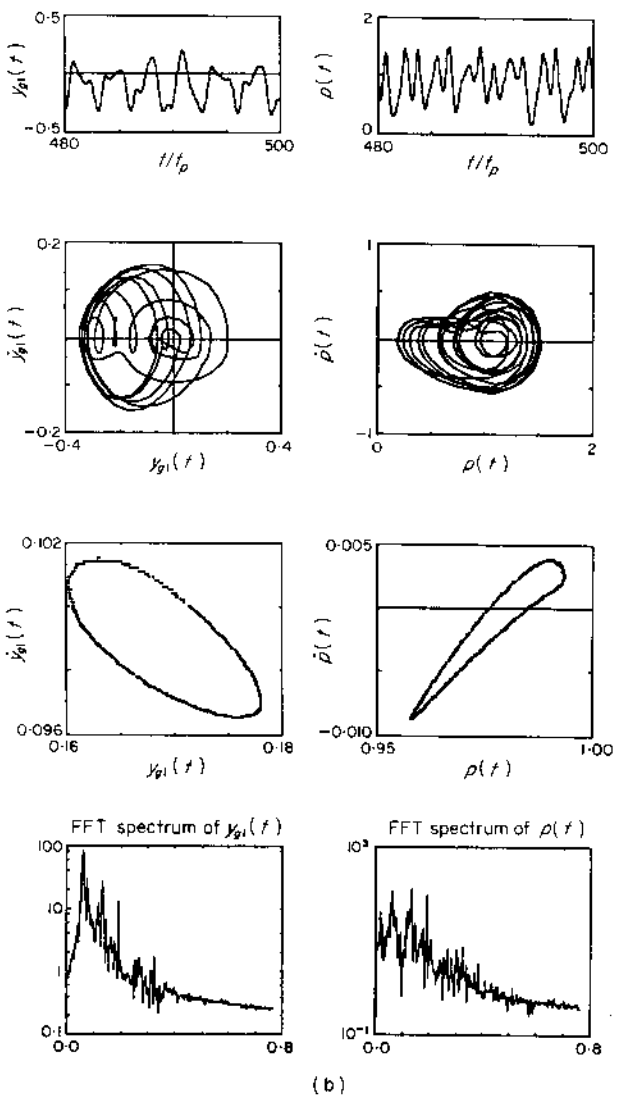

(b)

Figure 18—*continued.*

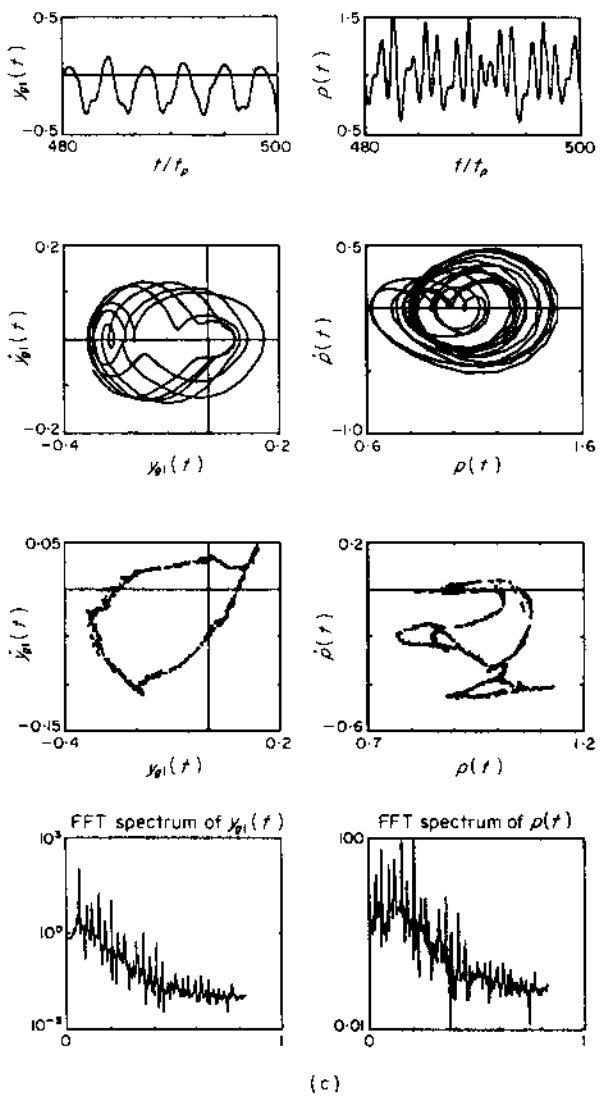

(c)

Figure 18—*continued.*

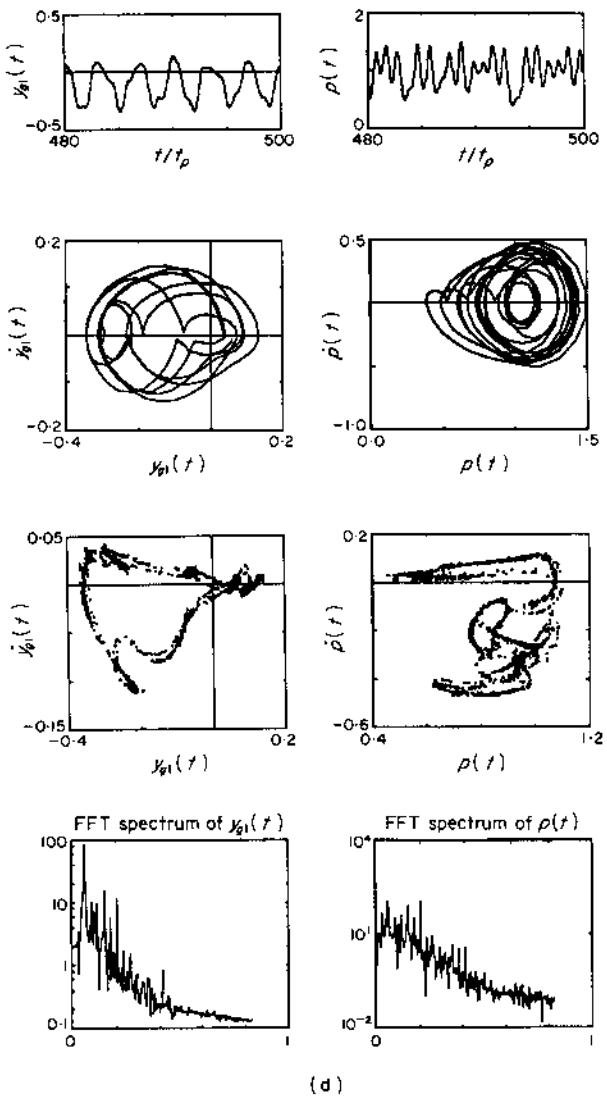

(d)

Figure 18—*continued.*

dictated by mostly transverse vibrations. Here, the bearing non-linearities affect the transverse displacements y_{g1} and y_{g2}, which makes the first mode non-linear. The second peak is more dependent on the modal interactions. Here, all of the solutions are again purely harmonic and only no-impact and single-sided impact regimes exist. However, an increase in $\hat{k}$ introduces chaotic and subharmonic responses, as shown in Figures 23(b), (c) and 24(b), (c). For instance, all the solutions within the range $0{\cdot}6 < \Omega_h < 1{\cdot}7$ are non-harmonic for $\hat{k} = 10$; the frequency response is no longer well defined and modal coupling is sufficiently strong so that jump discontinuities are observed at both peaks.

A decrease in F_m/F_{ah} enhances the degree of the non-linearity, as shown in Figures 25(a), (b) and 26(a), (b). At $F_m/F_{ah} = 1$ in Figures 25(b) and 26(b), the responses within

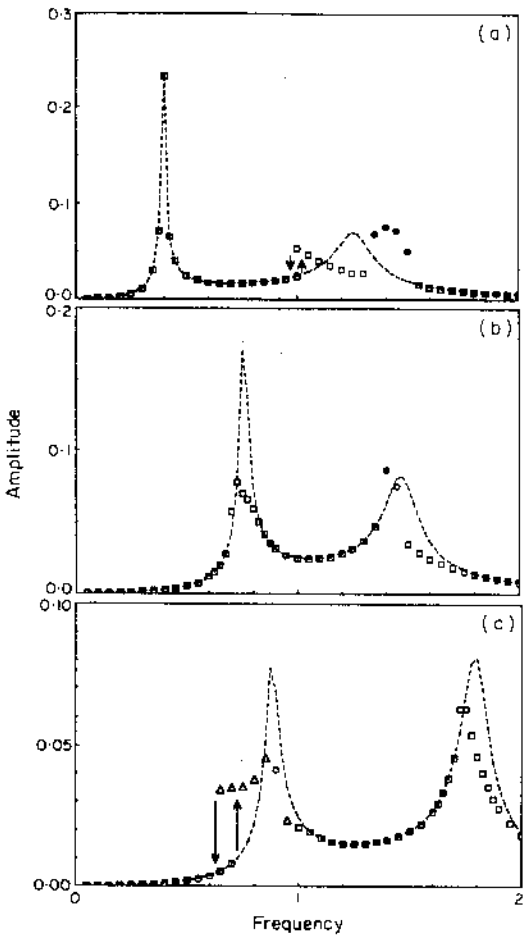

Figure 19. y_{gia} versus Ω_h plots for $F_m = 0{\cdot}1$, $F_{ah} = 0{\cdot}05$, $F_{bi} = 0$, $b_h = b_c = 0{\cdot}1$, $b_{bi} = 0$; (a) $\hat{k} = 1$; (b) $\hat{k} = 5$; (c) $\hat{k} = 10$; □, harmonic; △, period-one non-harmonic; ○, period-n subharmonic; ●, quasi-periodic or chaos; - - -, corresponding linear response.

$0{\cdot}5 < \Omega_h < 1{\cdot}4$ are scattered and non-harmonic. However, radial preloads F_{bi} on bearings should help the mean load F_m in limiting the effect of non-linearities. To prove this claim, we applied a high radial preload to both bearings, say $\bar{F}_m = \bar{F}_{bi}$, $i = 1, 2$, corresponding to $F_{bi} = 0{\cdot}25$ for $F_m = 1{\cdot}0$ in the dimensionless form, and compared results with the previous case of $F_{bi} = 0$, as shown in Figures 25(a), (c) and 26(a), (c). In Figures 25(c) and 26(c) it is shown that most of the subharmonic and chaotic solutions of Figures 25(a) and 26(a) are replaced by harmonic solutions. Hence a well defined frequency response curve with clear jump discontinuities is obtained by applying F_{bi}.

Finally, the roller bearings were replaced with ball bearings with $b_c = b_{bi} = 0{\cdot}001$ mm and again the effect of $\hat{k} = k_{bi}/k_h$ was investigated, with the results shown in Figures 27 and 28. With soft bearings ($\hat{k} = 1$) the frequency response is linear (no jumps), which indicates that there are no impacts within the frequency range considered as shown in Figures 27(a) and 28(a). However, at a larger value of $\hat{k}$, double-sided impact solutions appear since the clearance $2b_{bi}$ is very small. In Figures 27(b) and 28(b) for $\hat{k} = 5$, the frequency region of $0{\cdot}65 < \Omega_h < 0{\cdot}8$ consists of the double-sided solutions. When $\hat{k}$ is increased to 10, the same behavior is also seen at the second peak as shown in Figures

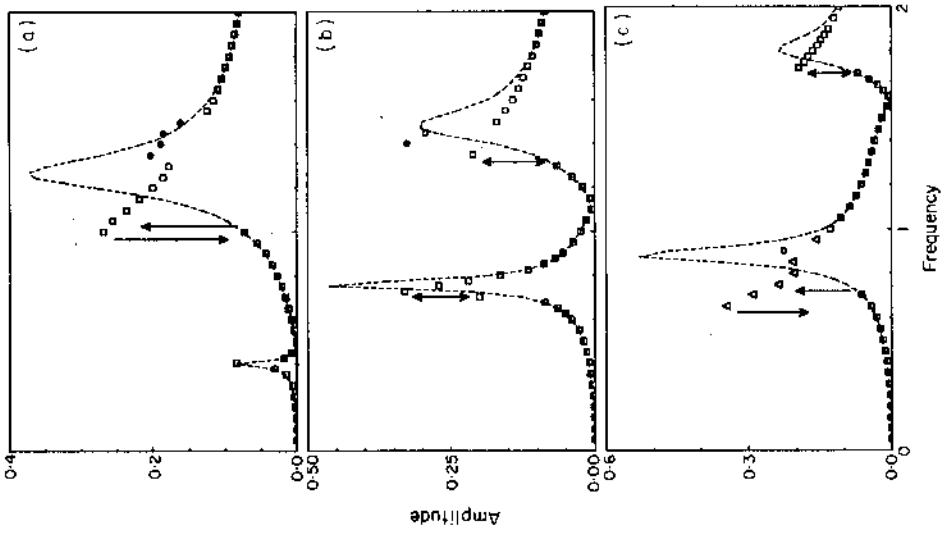

Figure 20. P_n versus Ω_h plots for $F_m = 0{\cdot}1$, $F_{ah} = 0{\cdot}05$, $F_{hi} = 0$, $b_h = b_c = 0{\cdot}1$, $b_{hi} = 0$; (a) $k = 1$; (b) $k = 5$; (c) $k = 10$; □, harmonic; △, period-one non-harmonic; ○, period-n subharmonic; ●, quasi-periodic or chaos; - - -, corresponding linear response.

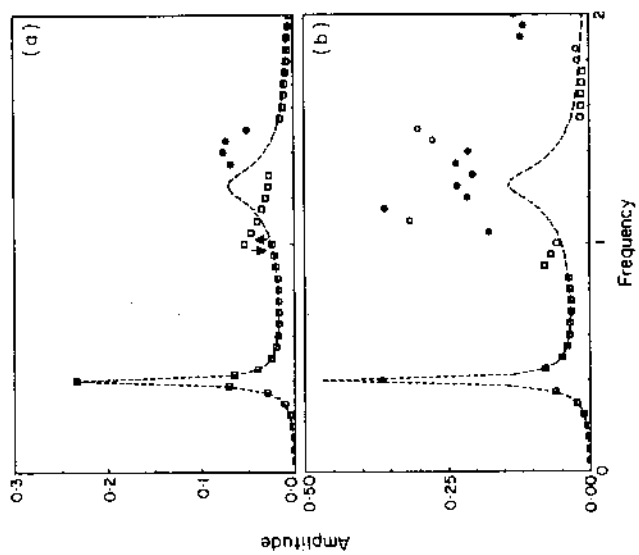

Figure 21. y_{RMS} versus Ω_h plots for $F_m = 0{\cdot}1$, $F_{hi} = 0$, $b_h = b_c = 0{\cdot}1$, $b_{hi} = 0$, $\zeta_{33} = 0{\cdot}05$, $\zeta_{13} = \zeta_{23} = 0{\cdot}0125$, $\zeta_{11} = \zeta_{22} = 0{\cdot}01$, $k = 1$; (a) $F_{ah} = 0{\cdot}05$; (b) $F_{ah} = 0{\cdot}1$; □, harmonic; ○, period-n subharmonic; ●, quasi-periodic or chaos; - - -, corresponding linear response.

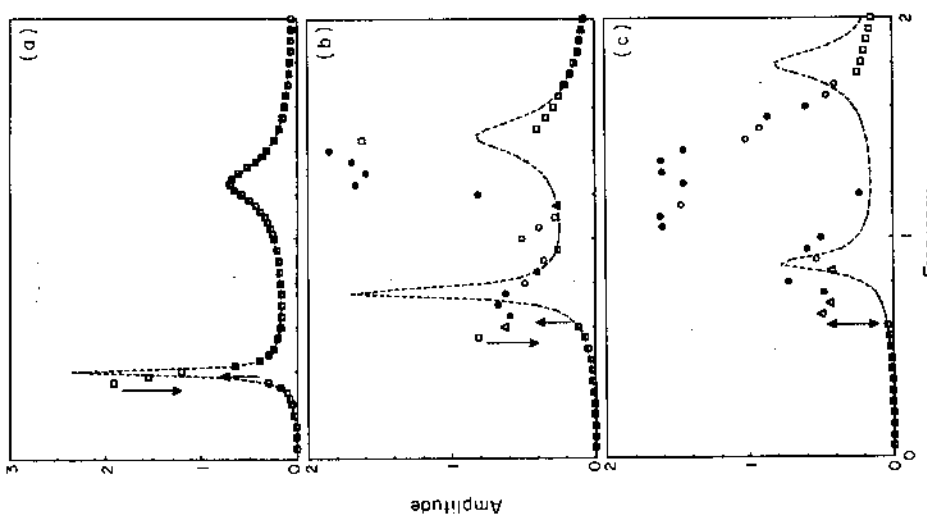

Figure 23. $y_{p/a}$ versus Ω_h plots for the case of roller bearings; $F_m = 1{\cdot}0$, $F_{ah} = 0{\cdot}5$, $F_{bi} = 0$, $b_h = 0$, $b_{bi} = b_c = 0{\cdot}01$ mm; (a) $\hat{k} = 1$; (b) $\hat{k} = 5$ (c) $\hat{k} = 10$; □, harmonic; △, period-one non-harmonic; ○, period-n subharmonic; ●, quasi-periodic or chaos; - - -, corresponding linear response.

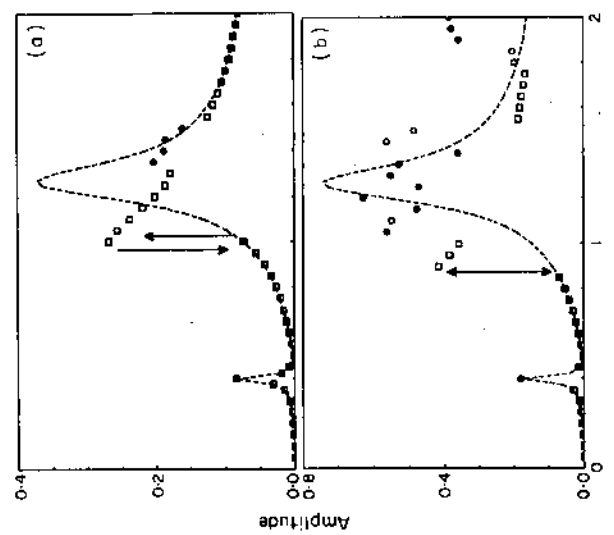

Figure 22. p_a versus Ω_h plots for $F_m = 0{\cdot}1$, $F_{bi} = 0$, $b_h = b_c = 0{\cdot}1$, $b_{bi} = 0$; $\hat{k} = 1$; (a) $F_{ah} = 0{\cdot}05$; (b) $F_{ah} = 0{\cdot}1$; □, harmonic; ○, period-n subharmonic, ●, quasi-periodic or chaos; - - - - -, corresponding linear response.

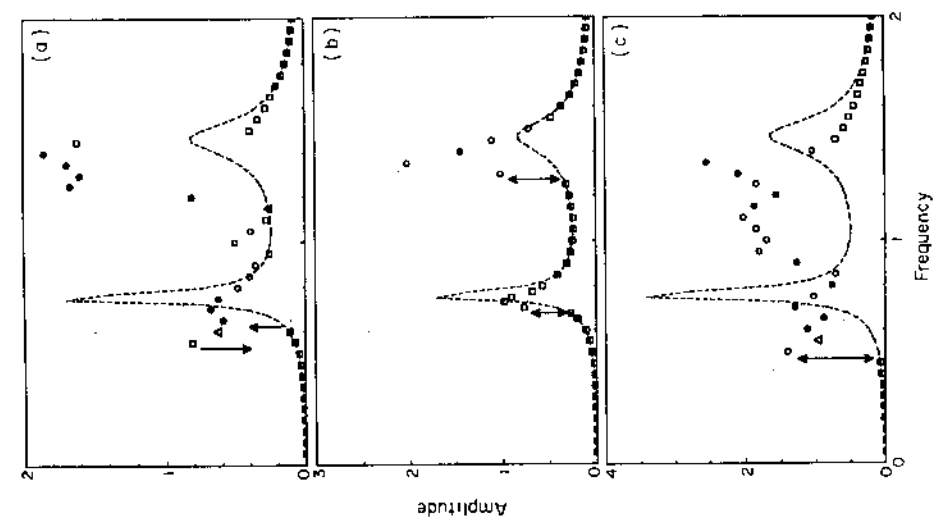

Figure 24. p_a versus Ω_h plots for the case of roller bearings; $F_{ai} = 1{\cdot}0$, $F_{ah} = 0{\cdot}5$, $F_{hi} = 0$, $b_h = 0$, $b_{hi} = b_c = 0{\cdot}01$ mm; (a) $k = 1$; (b) $k = 5$; (c) $k = 10$; □, harmonic; △, period-one non-harmonic; ○, period-n subharmonic; ●, quasi-periodic or chaos; - - -, corresponding linear response.

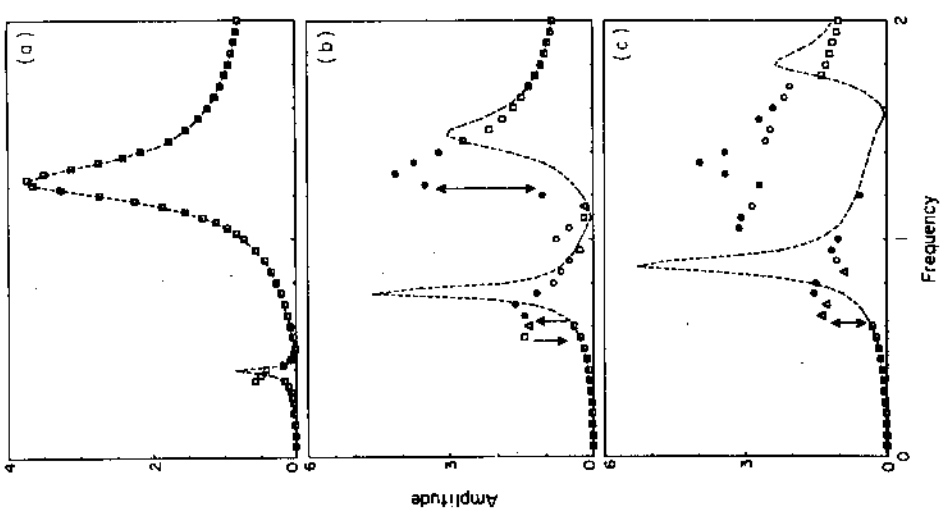

Figure 25. y_{gia} versus Ω_h plots for the case of roller bearings; $F_{ai} = 1{\cdot}0$, $b_h = 0$, $b_{hi} = b_c = 0{\cdot}01$ mm, $k = 5$; (a) $F_{ah} = 0{\cdot}5$, $F_{hi} = 0$; (b) $F_{ah} = 0{\cdot}5$, $F_{hi} = 0{\cdot}25$; (c) $F_{ah} = 1{\cdot}0$, $F_{hi} = 0$; □, harmonic; △, period-one non-harmonic; ○, period-n subharmonic; ●, quasi-periodic or chaos; - - -, corresponding linear response.

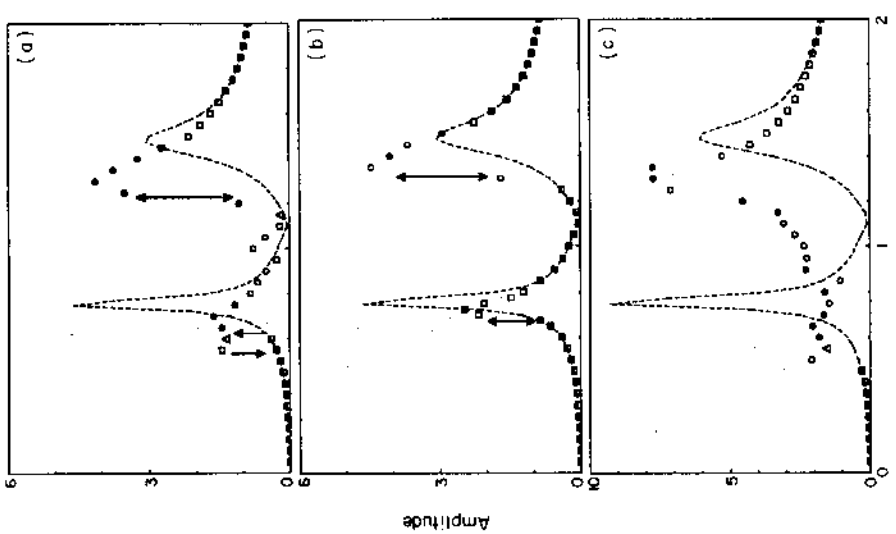

Figure 26. p_a versus Ω_h plots for the case of roller bearings; $F_m = 1{\cdot}0$, $b_h = 0$, $b_{hi} = b_r = 0{\cdot}01$ mm, $k = 5$; (a) $F_{ah} = 0{\cdot}5$, $F_{bi} = 0$; (b) $F_{ah} = 0{\cdot}5$, $F_{bi} = 0{\cdot}25$; (c) $F_{ah} = 1{\cdot}0$, $F_{bi} = 0$; □, harmonic; △, period-one non-harmonic; ○, period-n subharmonic; ●, quasi-periodic or chaos; - - -, corresponding linear response.

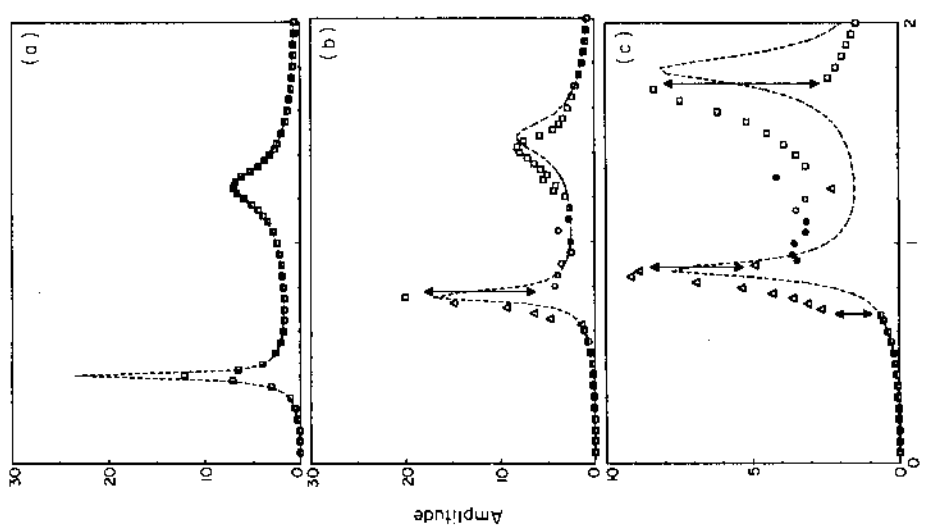

Figure 27. y_{gir} versus Ω_h plots for the case of deep-groove ball bearings; $F_m = 10$, $F_{ah} = 5$, $F_{bi} = 0$, $b_h = 0$, $b_{hi} = b_r = 0{\cdot}001$ mm; (a) $k = 1$; (b) $k = 5$; (c) $k = 10$; □, harmonic; △, period-one non-harmonic; ○, period-n subharmonic; ●, quasi-periodic or chaos; - - -, corresponding linear response.

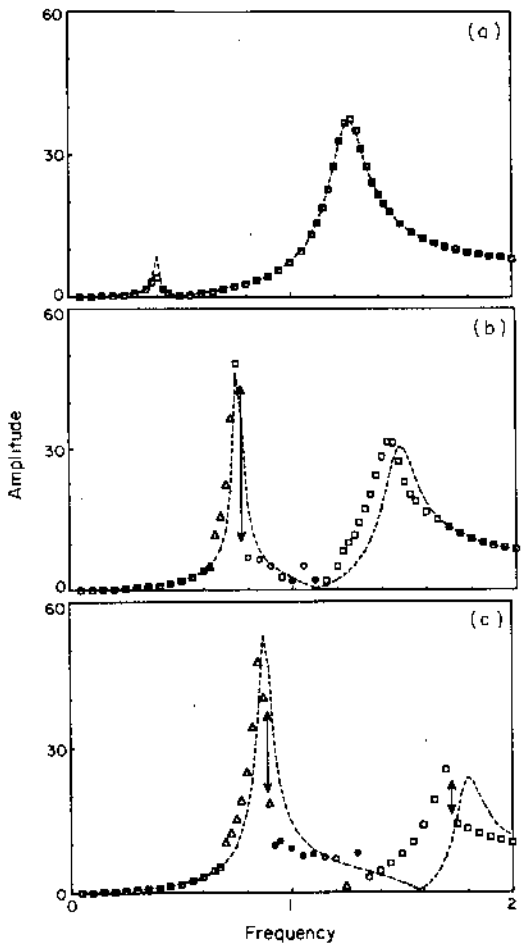

Figure 28. p_a versus Ω_h plots for the case of deep-groove ball bearings; $F_m = 10$, $F_{ah} = 5$, $F_{bi} = 0$, $b_h = 0$, $b_{bi} = b_c = 0{\cdot}001$ mm; (a) $\hat{k} = 1$; (b) $\hat{k} = 5$; (c) $\hat{k} = 10$; □, harmonic; △, period-one non-harmonic; ○, period-n subharmonic; ●, quasi-periodic or chaos; - - -, corresponding linear response.

27(c) and 28(c). The earlier discussion on the effect of F_{ah}/F_m and F_{bi}/F_m for roller bearings is also applicable to the ball bearings as well.

6. EXPERIMENTAL VALIDATION

Munro's experimental dynamic transmission error results [2], which were acquired in 1962 by using a four-square spur gear test rig, have been used earlier to validate our spur gear pair model [9] when the modes were weakly coupled with each other. Now, we can use the three-degree-of-freedom non-linear model of Figure 2(a) to analyze his test set-up [2]. In our analysis, bearings are assumed to be linear since they were highly preloaded; only gear backlash non-linearity is considered with $2b_h = 0{\cdot}12$ mm [39]. The system parameters used in equation (3a) under four different mean loads are listed in Table 2. The system damping ratios are assumed to be uniform at each load. Average mesh stiffness k_h and alternating load F_{ah} values associated with each mean load F_m are also tabulated in Table 2.

TABLE 2

Parameters of Munro's experimental set-up extracted from reference [2]

	Mean load, F_m			
	Design load (DL) 0·183	3/4 of DL 0·146	1/2 of DL 0·105	1/4 of DL 0·0579
F_{ah}	0·0058†	0·0178	0·0296	0·0393
k_b (N/m)	$1{\cdot}16\times10^9$	$1{\cdot}16\times10^9$	$1{\cdot}16\times10^9$	$1{\cdot}16\times10^9$
k_h (N/m)	$3{\cdot}44\times10^8$	$3{\cdot}22\times10^8$	$3{\cdot}01\times10^8$	$2{\cdot}72\times10^8$
κ_{11}, κ_{22}	0·950	0·966	0·983	1·007
κ_{13}, κ_{23}	0·242	0·242	0·242	0·242
ζ_{11}, ζ_{22}‡	0·01	0·01	0·01	0·01
ζ_{13}, ζ_{23}‡	0·00375	0·00375	0·00375	0·00375
ζ_{33}‡	0·015	0·015	0·015	0·015

† Modified so that the linear peak matches with the measured value.
‡ Estimated by using the experimental data of reference [2].

Dynamic transmission error predictions are compared with the measurements [2] in Figures 29–33. At the design load (DL), which corresponds to the minimum static transmission error, good agreement is seen except for the jump discontinuity found experimentally at the second peak. In our model, we have increased F_{ah} slightly beyond the value given in reference [2], so that the predicted amplitude of the first linear peak matches very well with the experiment. Such slight changes in critical system parameters such as F_{ah} and ζ, although they are varied within the experimental uncertainties, may alter the frequency response drastically, as illustrated in Figures 30(a) and 30(b). In Figure 30(a) we note that when we reduce the force ratio F_m/F_{ah} from 30 (the value given in reference [2]) to 10, a jump discontinuity at the second peak is seen which is compatible with the experiment. Similarly, a small change in the damping values, which are not reported in reference [2], also affects the frequency response, as shown in Figure 30(b). In Figures 31–33 are shown comparisons of the dynamic transmission error spectra at 3/4, 1/2 and 1/4 of the design load. From these spectra we conclude that our proposed

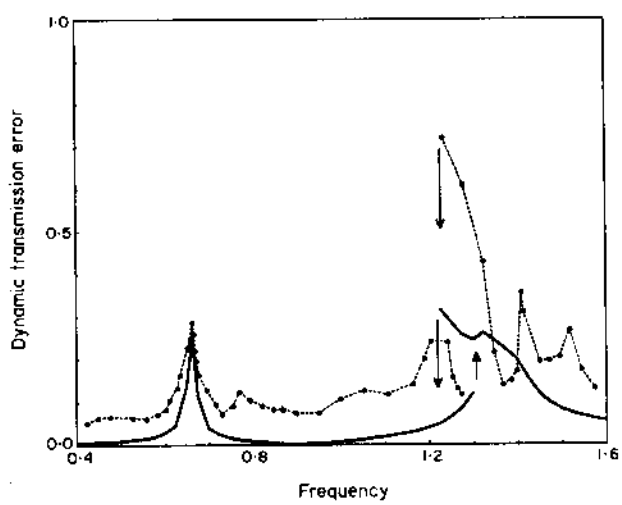

Figure 29. Comparison of theory (——) with Munro's [2] experiment (· · · ● · · ·) at the design load.

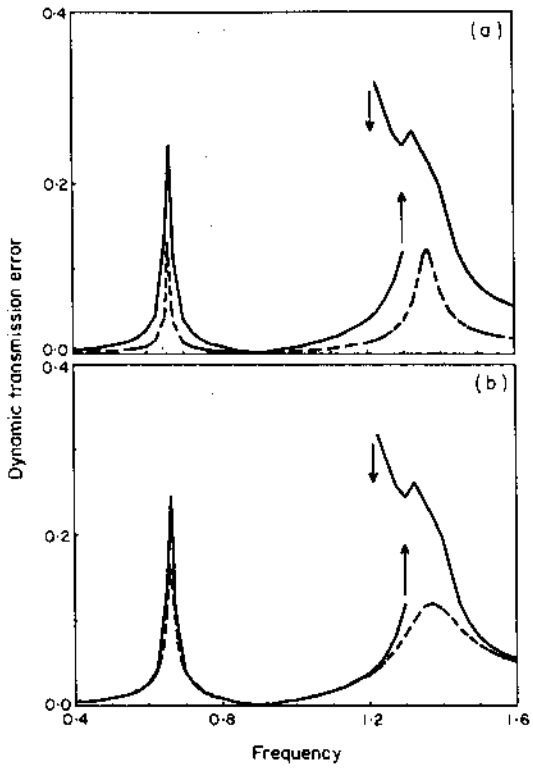

Figure 30. Effect of (a) alternating load (- - -, $F_m/F_{ah} = 30$; ———, $F_m/F_{ah} = 10$) and (b) damping (- - -, $\zeta_{33} = 0{\cdot}05$; ———, $\zeta = 0{\cdot}015$) on the dynamic transmission error spectrum at the design load.

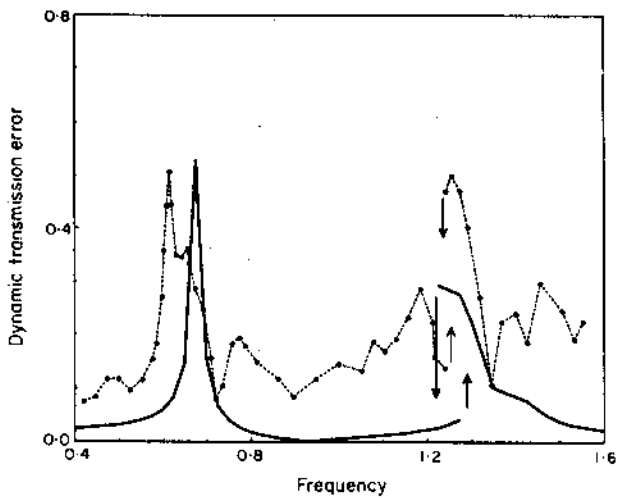

Figure 31. Comparison of theory with Munro's [2] experiment at 3/4 of the design load. Key as Figure 29.

theory agrees well with the experimental results of Munro [2] both qualitatively and quantitatively, although amplitudes in the off-resonance regions are slightly off. Such amplitudes are close to the noise floor in the experiment. Further, discrepancies between the theory and the experiment may be due to the assumptions made in this study. However, it should be pointed out that the experiment, even though it was very precise, was

conducted almost three decades back before the advent of modern non-linear dynamics and chaos science [31–36]. Interestingly, Munro [2] had also reported subharmonic responses at 3/4, 1/2 and 1/4 of the design load, and "unrepeatable responses" (probably chaos) at 1/4 of the design load. Our results agree with such experimental observations as well. Both experiment and theory show that the chaotic solutions dictate the frequency response beyond the second resonance for 1/4 of the deisgn load in Figure 33. This experimental facility is being re-installed and instrumented for further measurements [39]; a joint research program is being planned, based on the results of this paper.

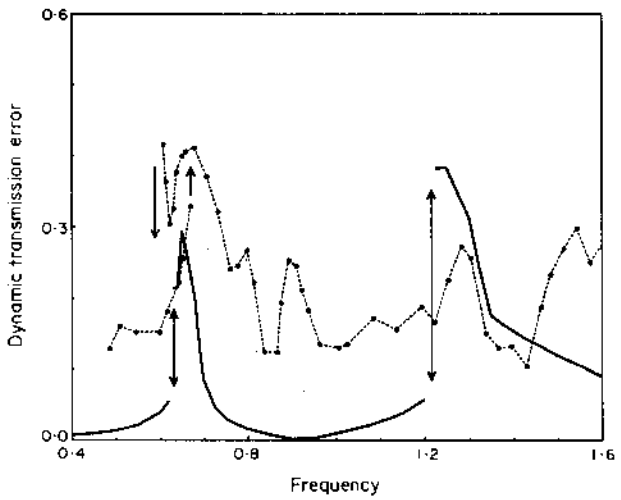

Figure 32. Comparison of theory with Munro's [2] experiment at 1/2 of the design load. Key as Figure 29.

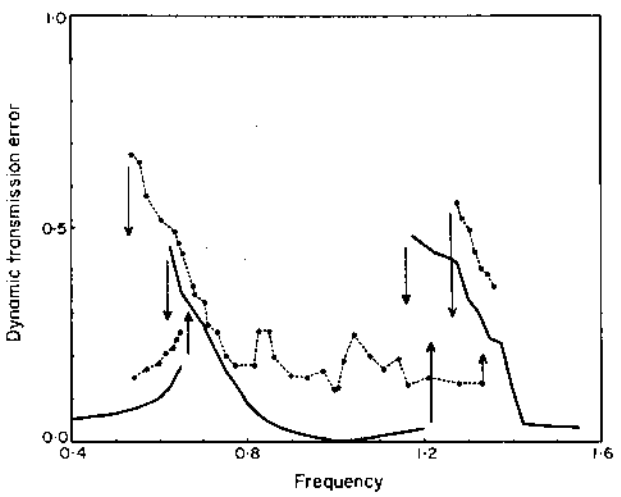

Figure 33. Comparison of theory with Munro's [2] experiment at 1/4 of the design load. Key as Figure 29.

7. CONCLUDING REMARKS

This analytical study on the non-linear dynamics of a geared rotor–bearing system with gear backlash and bearing clearances, as excited by the internal static transmission error and/or external torque pulsations, has made a number of contributions to the state of

the art. First, an approximate non-linear model of the rolling element bearings with clearances has been developed and validated. Second, our mathematical model has been validated as it compares well with a previous experimental study, and several key parameters such as the mean load, mean to alternating force ratio, radial bearing preload, bearing stiffness and damping have been identified. Third, conditions for the chaotic and subharmonic resonances, and the routes to chaos have been identified. Fourth, non-linear modal interactions have been examined. Finally, on a more fundamental note, our study enriches the current literature on coupled vibro-impact pairs [10, 13, 14].

Current research work is focused on the analysis of asymmetric geared systems, and on the inclusion of prime mover, load and time varying gear mesh stiffness in our proposed formulation. In future, we intend to examine single- and multi-mesh non-linear dynamic problems in other types of geared drives. Also, efforts are under way to measure the frequency response characteristics on the gear test facility [39], which will be used to verify or refine our theory further.

ACKNOWLEDGMENTS

We thank NASA Lewis Research Center for supporting this study, and D. R. Houser for his guidance.

REFERENCES

1. H. N. OZGUVEN and D. R. HOUSER 1988 *Journal of Sound and Vibration* **121**, 383–411. Mathematical models used in gear dynamics—a review.
2. R. G. MUNRO 1962 *Ph. D. Dissertation, University of Cambridge.* The dynamic behaviour of spur gears.
3. A. KUBO, K. YAMADA, T. AIDA and S. SATO 1972 *Transactions of the Japan Society of Mechanical Engineers* **38**, 2692–2715. Research on ultra high speed gear devices (reports 1–3).
4. K. UMEZAWA, T. SATA and J. ISHIKAWA 1984 *Bulletin of the Japan Society of Mechanical Engineers* **38**, 102–109. Simulation of rotational vibration of spur gears.
5. F. KUCUKAY 1984 *Proceedings of the Third Conference on Vibrations of Rotating Machinery, Institution of Mechanical Engineers*, 73–79. Dynamic loads in gear teeth.
6. T. SAKAI, Y. DOI, K. YAMATOMO, T. OGASAWARA and M. NARITA 1981 *SAE Paper* 810773. Theoretical and experimental analysis of rattling noise of automotive gearbox.
7. S. OHNUMA, Y. SHIGETARO, I. MINEICHI and T. FUJIMOTO 1985 *SAE Paper* 850979. Research on the idling rattle of manual transmission.
8. R. SINGH, H. XIE and R. J. COMPARIN 1989 *Journal of Sound and Vibration* **131**, 177–196. Analysis of an automotive neutral gear rattle.
9. A. KAHRAMAN and R. SINGH 1990 *Journal of Sound and Vibration* **142**, 49–75. Non-linear dynamics of a spur gear pair.
10. L. E. GALHOUD, S. F. MASRI and J. C. ANDERSON 1987 *Journal of Applied Mechanics, Transactions of the American Society of Mechanical Engineers* **54**, 215–225. Transfer function of a class of nonlinear multidegree of freedom oscillators.
11. H. WINTER and M. KOJIMA 1981 *Proceedings of the International Symposium on Gearing & Power Transmissions, Tokyo* c-12. A study on the dynamics of geared system—estimation of overload on gears in system.
12. H. H. LIN, R. L. HUSTON and J. J. COY 1987 *NASA Technical Memorandum* 100180. On dynamic loads in parallel shaft transmissions, I-modeling and analysis.
13. R. J. COMPARIN and R. SINGH 1990 *Journal of Sound and Vibration* **142**, 101–124. Frequency response characteristics of coupled impact pairs.
14. R. J. COMPARIN and R. SINGH 1990 *Journal of Mechanical Design, Transactions of the American Society of Mechanical Engineers* **112**, 237–245. An analytical study of automotive neutral gear rattle.
15. A. H. NAYFEH 1983 *Journal of Sound and Vibration* **90**, 237–244. The response of multi-degree-of-freedom systems with quadratic non-linearities to a harmonic parametric resonance.

16. A. G. HADDOW, A. D. S. BARR and D. T. MOOK 1984 *Journal of Sound and Vibration* **97**, 451–473. Theoretical and experimental study of modal interaction in a two-degree-of freedom structure.
17. D. T. MOOK, R. H. PLAUT and N. HAQUANG 1985 *Journal of Sound and Vibration* **102**, 473–492. The influence of an internal resonance on non-linear structural vibrations under subharmonic resonance conditions.
18. D. T. MOOK, N. HAQUANG and R. H. PLAUT 1986 *Journal of Sound and Vibration* **104**, 229–241. The influence of an internal resonance on non-linear structural vibrations under combined resonance conditions.
19. M. P. CARTMELL and J. W. ROBERTS 1988 *Journal of Sound and Vibration* **123**, 81–101. Simultaneous combination resonances in an autoparametric resonant system.
20. D. A. STREIT, A. K. BAJAJ and C. M. KROUSGRILL 1988 *Journal of Sound and Vibration* **124**, 297–314. Combination parametric resonance leading to periodic and chaotic response in two-degree-of freedom systems with quadratic non-linearities.
21. M. HORTEL 1967 *Proceedings of the Fourth Conference on Non-linear Oscillations*, 337–346. Forced damped vibrations in a nonlinear parametric system of gears with several degrees of freedom.
22. R. J. COMPARIN and R. SINGH 1989 *Journal of Sound and Vibration* **133**. Non-linear frequency response characteristics of an impact pair.
23. A. KAHRAMAN 1990 *Ph.D. Dissertation, Ohio State University*. Non-linear dynamic analysis of geared rotor-bearing systems with clearances.
24. D. R. HOUSER 1988 *Proceedings of Inter-Noise* 88, 601–606. Gear noise state of the art.
25. T. A. HARRIS 1966 *Rolling Bearing Analysis*. New York: John Wiley.
26. M. F. WHITE 1979 *Journal of Applied Mechanics, Transactions of the American Society of Mechanical Engineers* **46**, 677–684. Rolling element bearing vibration transfer characteristics: effect of stiffness.
27. T. C. LIM and R. SINGH 1990 *Journal of Sound and Vibration* **139**, 179–199. Vibration transmission through rolling element bearings, part I: bearing stiffness formulation.
28. A. KAHRAMAN, H. N. OZGUVEN, D. R. HOUSER and J. JAKRAJSEK 1989 *Proceedings of Fifth International Power Transmission and Gearing Conference, the American Society of Mechanical Engineers*, 375–382. Dynamic analysis of geared rotors by finite elements.
29. A. GELB and W. E. VANDER VELDE 1968 *Multiple Input Describing Functions and Nonlinear System Design*. New York: McGraw-Hill.
30. IMSL INC. 1986 *IMSL Users Manual*.
31. F. C. MOON 1987 *Chaotic Vibrations*. New York: John Wiley.
32. C. GREBOGI, E. OTT, S. PELIKAN and J. A. YORKE 1984 *Physica* **13D**, 261–268. Strange attractors that are not chaotic.
33. J. M. T. THOMPSON and H. B. STEWART 1986 *Nonlinear Dynamics and Chaos*. Chichester: John Wiley.
34. J. D. CRAWFORD and S. OMOHUNDRO 1984 *Physica* **13D**, 161–180. On the global structure of period doubling flows.
35. J. B. MCLAUGHLIN 1981 *Journal of Statistical Physics* **24**, 375–388. Period-doubling bifurcations and chaotic motion for a parametrically forced pendulum.
36. H. G. SCHUSTER 1984 *Deterministic Chaos*. Weinheim: Physik-Verlag.
37. A. KUBO 1989 Private communication.
38. J. KRAUS, J. J. BLECH and S. G. BRAUN 1987 *Journal of Vibration, Acoustics, Stress, and Reliability in Design, Transactions of the American Society of Mechanical Engineers* **109**, 235–240. *In situ* determination of rolling bearing stiffness and damping by modal analysis.
39. R. G. MUNRO 1989 Private communication.

APPENDIX: LIST OF SYMBOLS

b	backlash
c, C	viscous damping coefficient
d	diameter
e	static transmission error
f	non-linear displacement function
F	force

H total number of rolling elements in contact
I rotary inertia
k, K stiffness
m, M mass
n power of non-linear bearing function
N describing function
p relative displacement
q displacement
t time
T torque
v gear ratio
x relative displacement
y transverse displacement
Z number of rolling elements
α angular position of the rolling element in contact
δ Kronecker delta
ϕ phase angle
φ an angle
κ dimensionless stiffness
θ rotational displacement
ω natural frequency
Ω excitation frequency
ζ damping ratio
ψ mode shape

Subscripts

a alternating component
b bearing
$c, c1$ reference quantities
d dynamic
e external
$g1$ pinion
$g2$ gear
h gear mesh
i internal
L load
m mean component
n natural
p period
r mode index
s static or modal index
t inner contact
T torque
I, II, III modal index

Superscripts

$\overline{}$ dimensional quantities†
$\tilde{}$ amplitude of a harmonic function
$\dot{}$ derivative with respect to time
$\hat{}$ stiffness ratio

† All dimensionless quantities are without any superscript.